Modeling storage particle delamination and electrolyte cracking in cathodes of solid state batteries

Tao Zhang [a,*], Marc Kamlah [b], Robert M. McMeeking [a,c,d]

[a] Materials Department, University of California, Santa Barbara, CA 93106, USA
[b] Institute for Applied Materials, Karlsruhe Institute of Technology, 76344 Eggenstein-Leopoldshafen, Germany
[c] Department of Mechanical Engineering, University of California, Santa Barbara, CA 93106, USA
[d] School of Engineering, University of Aberdeen, King's College, Aberdeen AB24 3UE, Scotland, UK

ARTICLE INFO

Keywords:
Solid-state batteries
Interface delamination
Electrolyte cracking
Phase field model for fracture
Interfacial reaction

ABSTRACT

Interface delamination between storage particles and solid electrolytes contributes to greater impedance for Li transfer and capacity loss in solid-state batteries. Electrolyte cracking would cause degradation of the ionic or electronic conductivity of electrolytes. The occurrence of interface delamination and electrolyte cracking is commonly ascribed to mechanical stress, which evolves from inhomogeneous shrinkage and swelling of storage particles confined by the surrounding solid electrolytes when lithium is extracted or inserted. Here, a coupled model of Li diffusion, ionic conduction, interfacial reaction, mechanical stress and a phase field fracture approach is applied to investigate defect-initiated interface delamination and how cracks nucleate in electrolytes in a full 3D dynamical description for the first time. We find that unstable interface delamination is a very likely event during extraction. On the other hand, homogeneous delamination where the whole interface delaminates simultaneously, can happen for smaller interfacial defects with larger particle sizes and higher applied current densities. Larger interfacial defects delay the onset of delamination due to damage dependent interfacial reaction. More particle storage capacity can be utilized for smaller particle sizes and smaller interfacial defects prior to delamination. We further demonstrate electrolyte cracking can happen quite readily, and the electrolyte can break into several parts in only one insertion half cycle and even the appearance of full delamination.

1. Introduction

Although liquid electrolyte systems are of great importance currently, solid-state batteries (SSBs) present a promising technology for next-generation batteries due to their increased capacity and safety. Besides the replacement of toxic and flammable liquid electrolytes, solid electrolyte separators demonstrate the potential for suppressing the growth of dendrites on Li metal anode, thus leading to a significant improvement in energy density by the use of Li metal as the anode material (Yang et al., 2017; Lin et al., 2017). However, integrating solid electrolytes (SEs) with the other components of the battery brings a significant challenge in SSBs (Janek and Zeier, 2016; Pasta et al., 2020). As shown in Fig. 1a, a typical SSB structure includes a Li metal anode, a composite solid-state cathode and a SE separating the electrodes. Composite cathodes in SSBs usually consist of the storage particles made of the active material (AM), surrounded by the SE to support ionic transport.

When Li is extracted from or inserted into the storage particles of the cathode, the storage particles undergo volumetric expansion/contraction, due to the constraint of SEs, leading to generation of possibly high stresses. As a result, transfer of

* Corresponding author.
E-mail address: taozhang@ucsb.edu (T. Zhang).

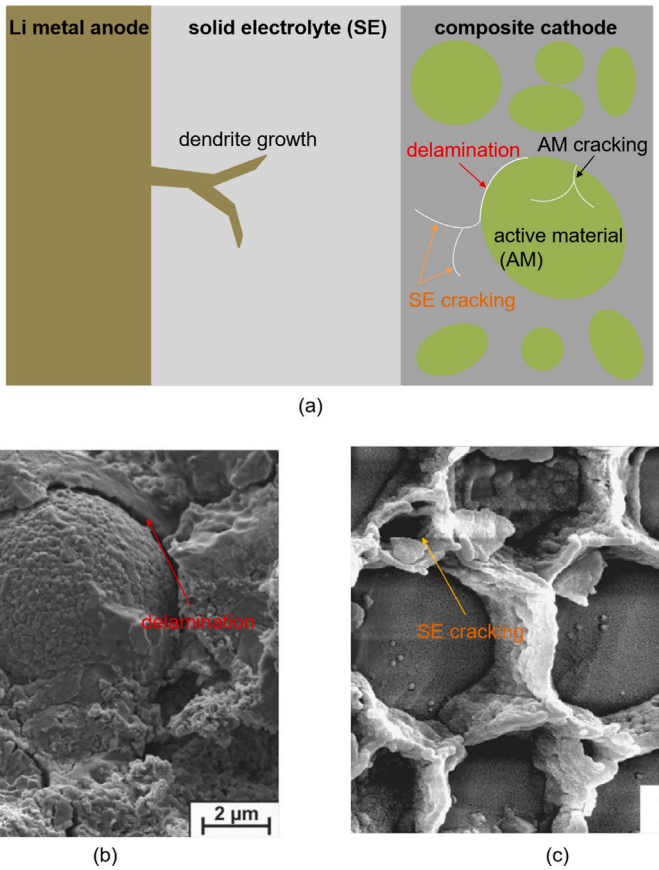

Fig. 1. (a) Schematics of a solid-state battery composed of Li metal anode, solid-state electrolyte separator and composite cathode, as well as its degradation mechanisms. (b) SEM image of interface delamination (Koerver et al., 2017) (Reprinted with permission from American Chemical Society). (c) SEM image of SE cracking (Cheng et al., 2017) (Reprinted with permission from Elsevier).

stresses through SEs could cause a complex coupled electro-chemo-mechanical behavior, which may lead to the fracture of storage particles (Zhang et al., 2018), SE cracking (Cheng et al., 2017), or delamination of the interface between the two (Koerver et al., 2017), see Fig. 1. It is probable that interface delamination causes greater impedance for transfer of Li and its ions at that interface, and thus leads to power fade in SSBs (Koerver et al., 2017). Fracture of SE in the cathode adjacent to AM seems to be less common than delamination of the interface between AM and SE. In ceramic electrolytes, however, cracking is a relevant possibility. It can be expected that degradation of the ionic or electronic conductivity of SE is a consequence of crack propagation in SE. In addition, cracking of SE may be paths along which lithium dendrites and filaments can grow (Porz et al., 2017). Although dendrites and filaments would be more likely to penetrate from the anode rather than the cathode, it is possible that cracks in SE in the cathode could be nuclei for lithium dendrites and filaments (Deshpande and McMeeking, 2023). Detailed insight into the problems of interface delamination and SE cracking thus has the potential to provide a central key to improving SSBs design and operation for future generations.

Most works related to chemo-mechanical fracture modeling focus on the AM (Huggins and Nix, 2000; Bhandakkar and Gao, 2010; Xu and Zhao, 2018; Klinsmann et al., 2015a, 2016b, 2015b, 2016a; Miehe et al., 2016; Zuo and Zhao, 2015; Xu et al., 2016; O'Connor et al., 2016; Mesgarnejad and Karma, 2019). By extension of the concepts of Huggins and Nix (2000), Bhandakkar and Gao (2010) studied an initially crack-free thin strip under a galvanostatic flux. They allowed the nucleation of cracks using a cohesive zone model, and determined a minimum particle size against comminution. Xu and Zhao (2018) recently exploited the cohesive zone model to study the corrosive fracture of electrodes within the theoretical framework of coupled diffusion and large deformation. They concluded that the wait-and-go behavior in the delayed fracture zone depends on the chemomechanical load and the supply of Li to the crack tip. Different from the cohesive zone models that restrict the crack to penetration along the corresponding element edges (Ortiz and Pandolfi, 1999; Xu and Needleman, 1994), the phase field method describes the crack as a smoothed continuum approximation rather than as a geometric feature with a physical discontinuity. The phase field method for fracture is therefore regarded as a promising tool to study complex crack propagation and the complicated paths that such cracks can follow Miehe et al. (2010), Borden et al. (2014). With the help of the phase field fracture method, Klinsmann et al. (2015a, 2016b, 2015b, 2016a) performed extensive analysis of crack propagation in brittle storage particles that contain pre-existing cracks,

with lithiation swelling and shrinkage leading to stresses in particles. During lithium insertion into 2D cylindrical particles with a circular cross section and into 3D spherical particles, Klinsmann et al. (2016b) identify conditions that lead to unstable crack growth, particle breakage, and crack branching, respectively. These events depend on the insertion rate and the particle size, with high insertion rates and large size making particles more prone to comminution. They find it necessary to include inertial dynamics in simulations to capture the inertia driven crack propagation. Klinsmann et al. (2015b) also find that crack growth during extraction initiates under less severe conditions than during insertion, while complete particle breakage is not observed during their simulations of lithium extraction. Mesgarnejad and Karma (2019) studied crack propagation of cathodic active particles using the phase field fracture method and quantified the relationships between stable or unstable crack propagation, initial crack size, and charging rate for 2D disks and 3D spherical particles during extraction.

The chemo-mechanical fracture modeling of solid-state cathodes remains a largely unexplored research avenue. Bucci et al. (2018) used a 1D spherically symmetric model based on a cohesive zone analysis to study homogeneous delamination at the interface between cathode storage particles and SEs in the absence of initial defects, where interface delamination is induced by storage particle shrinkage due to delithiation. Based on adhesive strengths for the interface ranging from 2 to 20 GPa, they find a threshold in terms of Young's modulus of the SE below which delamination will not happen, and a threshold in terms of interface toughness above which the same will not occur. It should be noticed that defect-initiated interface delamination is more possible than homogeneous interface delamination where the whole interface delaminates simultaneously (Deshpande and McMeeking, 2023). Bucci et al. (2017b) presented the first quantitative analysis of SE cracking caused by insertion-induced swelling of the storage particles in 2D. They investigated the fracture of SE based on the cohesive zone model, and simulated the behavior of storage particles having a square cross section embedded in a matrix of electronically conductive SE. The SE matrix is endowed with cohesive zones, and cracks propagate along them when the stress induced by swelling of the storage particle upon lithiation is large enough. They find that SEs with low elastic moduli are more prone to cracking, which runs counter to the concept that SEs with high elastic moduli would be more prone to SE cracking (Sakuda et al., 2013b; McGrogan et al., 2017). Their counterintuitive findings seem to be due to high deviatoric stress in the SE near the sharp corners of the storage particles triggering fracture in the cohesive zones. Thus, this problem may not occur when the storage particles are closer to spherical in shape (Deshpande and McMeeking, 2023). In addition, they neither insert initial cracks in the SE, nor do they provide a model for how cracks nucleate in the SE, other than by the cohesive stress in the cohesive zone being surpassed. As the cohesive stress they use is a modest value of 10 MPa, compared to a SE Young's modulus of 15 GPa, the cohesive zone appears to be too weak in regard to truly representing how cracks will nucleate in the SE. Bistri and Di Leo (2021) formulated a theoretical framework, which captures chemo-mechanical multi-particle interactions in electrode microstructures, including the potential for cohesive failure. A novel chemo-mechanical interface element is developed to include the Butler–Volmer reaction kinetics and concurrent potential for mechanical degradation. They studied the influence of storage particle size and AM volume fraction on solid-state cathode capacity and impedance, and find that storage particle delamination from the SE reduces electrode particle storage capacity and increases impedance. To the best of our knowledge, no works have reported the electro-chemo-mechanical fracture modeling of solid-state cathodes to investigate interface delamination and SE cracking in a full 3D dynamical description. For a comprehensive review of electro-chemo-mechanical modeling of all-solid-state batteries, see Deshpande and McMeeking (2023), Bistri et al. (2021). Notice that we focus on solid-state cathodes in this work, while dendritic cracking in the SE adjacent to the Li metal anode is beyond the scope of the current work. Please refer to Mukherjee et al. (2023), Klinsmann et al. (2019), Shishvan et al. (2020a,b), Bistri and Di Leo (2023) for details regarding the modeling of this aspect.

In this work, an extensive study on modeling storage particle delamination and electrolyte cracking in cathodes of SSBs during both Li extraction and insertion is conducted. For this, we develop an electro-chemo-mechanical fracture model of Li diffusion, ionic conduction, electrochemical reaction, mechanical stress and a phase field fracture approach for the storage particle surrounded by the SE, which encloses for the first time a full 3D dynamical description of interface delamination and SE cracking. Inertial dynamics, which plays a nontrival role on complex fracture phenomena, such as, crack branching and complete breakage, is incorporated into our model. This aspect has been ignored in the literature on fracture of solid-state electrodes. Different from the cohesive zone models in the literature, we exploit the phase-field fracture approach, in an exhaustive series of full 3D simulations without imposing any symmetry assumptions, to present defect-initiated interface delamination and how cracks nucleate in the SE. We find that interface delamination happens in an unstable way during extraction. We determine during extraction when homogeneous delamination will occur, and when additional cracks at the interface will be nucleated. These events are dependent on the imposed current density at the SE surface, the initial crack size, and the particle size, with higher current densities, smaller initial crack sizes and larger particle sizes making the interface more prone to delamination. Both our simulations and analytic considerations indicate that interface delamination is a very likely event. We further demonstrate that SE cracking can happen quite readily during insertion, which is consistent with analytic considerations. Intricate fracture phenomena, including crack branching and SE breakage, can break the SE into several parts in just one-half insertion cycle. We also identify conditions during insertion that lead to complete interface delamination. We emphasize that these findings are a unique result of the capabilities of the model, i.e., the simultaneous consideration of the evolution of the Li concentration in the AM, current density in the SE, interfacial reaction, mechanical stress, crack growth and inertia effects. Due to the numerical complexity of simulating fracture in a multi-physical problem, especially in 3D, advanced numerical technologies for time step adaptivity, as well as parallelization, are employed on a high-performance Linux computer cluster.

This paper is organized as follows: in the Model Formulation section, we formulate an electro-chemo-mechanical-fracture model for a storage particle surrounded by SE. In the Numerical Implementation section, we outline material parameters and numerical details. In the Results and Discussion section, we first validate the proposed model by comparing numerical results against analytical solution, and then focus on exhaustive series of studies of full 3D spherical particles embedded in SE. Different crack phenomena are investigated during extraction and insertion. Finally, we conclude our study in the Conclusion section.

2. Model formulation

Here we will formulate models for the SE, the storage particle and the interface between them, respectively. It is assumed that both the SE and the storage particle are isotropic linear elastic materials. Constitutive relations are given in terms of the small strain tensor

$$\epsilon_{ij} = \frac{1}{2}\left(u_{i,j} + u_{j,i}\right) \tag{1}$$

with u_i being the displacement vector. As a standard feature of a phase field fracture method, we introduce a damage variable d to indicate the two states referring to cracked and intact material, corresponding to order parameter values 1 and 0 respectively. To describe interface delamination and SE cracking, the damage variable is defined in the SE.

2.1. Solid electrolyte

The SE is considered as a single ion conductor, in which only the lithium ions are mobile, such that the counter ions are immobilized within it. Charge neutrality is also invoked in the SE, which is a good approximation to reality in almost all situations (Ganser et al., 2019a; Mykhaylov et al., 2019). Due to the condition of charge neutrality, the individual concentration c^+ can be replaced by a salt concentration c_s. The balance of mass provides

$$\frac{\partial c_s}{\partial t} = \operatorname{div} \vec{J}^+, \tag{2}$$

and the flux of the cation is given by

$$\vec{J}^+ = \frac{\vec{i}}{F}, \tag{3}$$

where F is the Faraday constant and $\vec{i}$ is the ionic current. An arbitrarily located crack in the SE may hamper ionic conduction perpendicular to the crack faces in a significant way, but ionic conduction parallel to the crack faces may less be hindered by the crack. Such an effect can be approximated by usage of the gradient of the damage variable (Klinsmann, 2016), such that the ionic current $\vec{i}$ reads as

$$\vec{i} = -\frac{1}{F}((1-d)^{\alpha}\kappa_0 + d^{\alpha}(\beta_1 \boldsymbol{D} + \beta_2(\boldsymbol{I} - \boldsymbol{D})\kappa_0))\vec{\nabla}\omega_+, \tag{4}$$

with $\alpha > 0$. Here $\boldsymbol{D} = (\vec{\nabla}d \otimes \vec{\nabla}d)/d^2$ is a tensor projecting onto the direction of the damage variable gradient. Hence, at the location of the crack, the effective ionic conductivity can be written as $\kappa_1 = d^{\alpha}\beta_1\kappa_0$ perpendicular to the crack faces and $\kappa_2 = d^{\alpha}\beta_2\kappa_0$ parallel to the crack faces. As a result, the ionic conductivity is reduced at locations of non-zero order parameter, with the relative reduction being determined by β_1 and β_2 confined to the range 0 to 1.

The gradient of electrochemical potential is (Ganser et al., 2019a; Deshpande and McMeeking, 2023)

$$\vec{\nabla}\omega_+ = \frac{RT}{c_s}\vec{\nabla}c_s - F\mathbb{E} - \Omega_+\vec{\nabla}T_H^{se}, \tag{5}$$

where $\mathbb{E}$ is the electric field, Ω_+ is the partial molar volume of the cation, and T_H^{se} is the hydrostatic stress in the SE. According to Eq. (5), the driving force for cation migration is the concentration gradient, the electric field and the stress gradient. Due to charge neutrality and the stability of the counterion, the composition of the material changes only negligibly during the conduction process. Thus, the concentration gradient as well as swelling and shrinkage of a single ion conductor are usually negligible ($\Omega_+ = 0$). As a consequence, cation migration is driven only by the electric field.

Combining Eqs. (2)–(5) yields

$$\operatorname{div}(((1-d)^{\alpha}\kappa_0 + d^{\alpha}(\beta_1 \boldsymbol{D} + \beta_2(\boldsymbol{I} - \boldsymbol{D})\kappa_0))\mathbb{E}) = 0. \tag{6}$$

The mass balance is therefore represented by the charge balance, and ionic conduction in a single ion conductor is purely ohmic. We further assume the system free energy of an arbitrary part P_{se} of the SE body in the form

$$\begin{aligned}\Psi_{se} &= \int_{P_{se}} \psi_{se}(d, \vec{\nabla}d, \boldsymbol{\epsilon}, \mathbb{D})dV \\ &= \int_{P_{se}} (\psi_{se}^F(d, \vec{\nabla}d) + \psi_{se}^M(d, \boldsymbol{\epsilon}) + \psi_{se}^E(\mathbb{D}))dV.\end{aligned} \tag{7}$$

The fracture free energy density (Miehe et al., 2010)

$$\psi_{se}^F = G_c \underbrace{\left(\frac{1}{2l}d^2 + \frac{l}{2}|\vec{\nabla}d|^2\right)}_{\gamma_l(d)} \tag{8}$$

approximates the fracture energy through replacement of the integration along the crack surface by a volume integration of the crack surface density $\gamma_l(d)$. G_c is the Griffith-type critical energy release rate of the SE. The phase field fracture method is a spatially smoothed representation of the crack, and the discrete crack is recovered when the length scale parameter l approaches zero.

Since compressive stress should not lead to crack growth, the elastic energy density $\psi_{se}^{M}(d,\boldsymbol{\varepsilon})$ is decomposed into compressive and tensile parts via (Miehe et al., 2010; Borden et al., 2012)

$$\psi_{se}^{\pm}(\boldsymbol{\varepsilon}) = \frac{L_{se}}{2}\langle \mathrm{tr}[\boldsymbol{\varepsilon}]\rangle_{\pm}^{2} + G_{se}\,\mathrm{tr}[\langle\boldsymbol{\varepsilon}\rangle_{\pm}^{2}]. \tag{9}$$

The angle brackets are defined by $\langle x\rangle_{\pm} = \frac{1}{2}(|x| \pm x)$ for scalars, and $\langle \boldsymbol{A}\rangle_{\pm} = \sum_i \langle\alpha_i\rangle_{\pm}\,\vec{r}_i \otimes \vec{r}_i$ for second order tensor quantities, where α_i and $\vec{r}_i$ are the eigenvalues and the corresponding eigenvectors of $\boldsymbol{A}$ respectively. L_{se} is the Lamé constant and G_{se} is the shear modulus of the SE. To model the release of elastic energy at cracked locations, we then multiply the tensile part ψ_{se}^{+} with a damage function, which becomes zero if the damage variable d approaches unity, so that

$$\psi_{se}^{M}(d,\boldsymbol{\varepsilon}) = [(1-d)^2 + k]\psi_{se}^{+}(d,\boldsymbol{\varepsilon}) + \psi_{se}^{-}(d,\boldsymbol{\varepsilon}), \tag{10}$$

where k is a numerical parameter for stabilizing the solution. The ordinary isotropic linear elastic energy density is recovered for $d = 0$ and $k = 0$.

For the sake of simplicity, we employ the isotropic formulation of electrostatics related to the electric displacement $\mathbb{D}$ (Ganser et al., 2019a)

$$\psi_{se}^{E}(\mathbb{D}) = \frac{1}{2\epsilon_0\epsilon_r}\mathbb{D}\cdot\mathbb{D}, \tag{11}$$

where ϵ_0 and ϵ_r are the vacuum and relative permittivity, respectively.

To derive the driving force for damage evolution, strain and electric displacement, we carry out the variation of the system free energy

$$\begin{aligned}\delta\Psi_{se} &= \int_{P_{se}} \Big(\frac{G_c^{se}}{l}d\;\delta d + G_c^{se}\;l\;\vec{\nabla}d\cdot\delta\vec{\nabla}d + \frac{\partial\psi_{se}^{M}}{\partial d}\;\delta d + \frac{\partial\psi_{se}^{M}}{\partial\boldsymbol{\varepsilon}} : \delta\boldsymbol{\varepsilon} + \frac{\partial\psi_{se}^{E}}{\partial\mathbb{D}}\cdot\delta\mathbb{D}\Big)\,dV \\ &= \int_{P_{se}} \left[\left(\frac{G_c^{se}}{l}d - G_c^{se}\;l\;\nabla^2 d - 2(1-d)\psi_{se}^{+}\right)\delta d + \frac{\partial\psi_{se}^{M}}{\partial\boldsymbol{\varepsilon}} : \delta\boldsymbol{\varepsilon} + \left(\frac{1}{\epsilon_0\epsilon_r}\mathbb{D}\right)\cdot\delta\mathbb{D}\right]\,dV \\ &\quad + \int_{\partial P_{se}} G_c^{se}\;l\;\vec{\nabla}d\cdot\vec{n}\;\delta d\;\,dA.\end{aligned} \tag{12}$$

Eq. (12) yields the natural boundary condition on the entire boundary ∂P_{se} as

$$\vec{\nabla}d\cdot\vec{n} = 0. \tag{13}$$

The driving force for damage evolution Y_{se} is defined as the variational derivative of the system free energy with respect to the damage variable d

$$Y_{se} = \frac{\delta\Psi_{se}}{\delta d} = \frac{G_c^{se}}{l}d - G_c^{se}\;l\;\nabla^2 d - 2(1-d)H_{se}. \tag{14}$$

where the local history field of maximum positive elastic stored energy

$$H_{se} = \max_{[0,t]}(\psi_{se}^{+}) \tag{15}$$

replaces ψ_{se}^{+} to ensure that the crack growth is irreversible so that no crack healing can occur. Thus, the evolution equation of damage variable d is given by

$$\eta\dot{d} = -Y_{se} = 2(1-d)H_{se} - \Big(\frac{G_c}{l}d - G_c^{se}\;l\;\nabla^2 d\Big), \tag{16}$$

where $\eta \geq 0$ is the viscosity parameter for stabilizing the numerical treatment (Miehe et al., 2010, 2016). Notice that the rate-independent limit case, where crack driving force $(2(1-d)H_{se})$ is in equilibrium with geometric crack resistance $(\frac{G_c}{l}d - G_c^{se}\;l\;\nabla^2 d)$, can be recovered when $\eta = 0$.

Similarly, mechanical stress $\mathbf{T}_{se}$ is defined as the variational derivative of the system free energy with respect to the strain $\boldsymbol{\varepsilon}$

$$\mathbf{T}_{se} = \frac{\partial\psi_{se}^{M}}{\partial\boldsymbol{\varepsilon}} = [(1-d)^2 + k]\frac{\partial\psi_{se}^{+}}{\partial\boldsymbol{\varepsilon}} + \frac{\partial\psi_{se}^{-}}{\partial\boldsymbol{\varepsilon}} = [(1-d)^2 + k]\mathbf{T}_{se}^{+} + \mathbf{T}_{se}^{-} \tag{17}$$

with

$$\mathbf{T}_{se}^{\pm} = L_{se}\langle\mathrm{tr}[\boldsymbol{\varepsilon}]\rangle_{\pm}\mathbf{I} + 2G_{se}\langle\boldsymbol{\varepsilon}\rangle_{\pm}. \tag{18}$$

Mechanical stress obeys conservation of linear momentum

$$\mathrm{div}\,\mathbf{T}_{se} = \rho_{se}\frac{\partial^2\vec{u}}{\partial t^2}, \tag{19}$$

where the term related to the material density of the SE ρ_{se} represents dynamic effects resulting from the inertia of the SE.

The electric field $\mathbb{E}$ is defined as the variational derivative of the system free energy with respect to the electric displacement $\mathbb{D}$

$$\mathbb{E} = \frac{\partial\psi_{se}^{E}}{\partial\mathbb{D}} = \frac{1}{\epsilon_0\epsilon_r}\mathbb{D}. \tag{20}$$

To satisfy Maxwell's equation ($\mathrm{curl}(\mathbb{E}) = \vec{0}$), the electric potential Φ is defined as

$$\mathbb{E} = -\vec{\nabla}\Phi, \tag{21}$$

which is governed by the charge balance (6).

2.2. Storage particles

Due to uncharged species in storage particles only mass transport due to chemo-mechanics remains. The free energy density of the storage particle is given by

$$\psi_{am}(c, \boldsymbol{\varepsilon}) = \psi_{am}^{C}(c) + \psi_{am}^{M}(c, \boldsymbol{\varepsilon}), \tag{22}$$

where the chemical energy density $\psi_{am}^{C}(c)$ is given by

$$\psi_{am}^{C}(c) = \mu_0 c + RTc_{max}\left((c/c_{max})\ln(c/c_{max}) + \left(1 - c/c_{max}\right)\ln\left(1 - c/c_{max}\right)\right). \tag{23}$$

Here, c is the Li concentration in the storage particle, which can be scaled with the maximum lithium concentration c_{max}. R and T are the universal gas constant and the temperature, respectively. The first term on the right hand side of Eq. (23) is the reference chemical potential of Li in the storage particle, and the terms related to temperature T represent the entropy of mixing, resulting from the disorder of Li-ions in the host lattice. Notice that one can include an enthalpic contribution to account for phase changes (Zhang et al., 2023).

The elastic strain energy density ψ^{e}, which defines the coupling between diffusion and mechanics, is given by

$$\psi^{M}(c, \boldsymbol{\varepsilon}) = \frac{L}{2}(\mathrm{tr}[\boldsymbol{\varepsilon} - \boldsymbol{\varepsilon}^{s}])^2 + G\,\mathrm{tr}[(\boldsymbol{\varepsilon} - \boldsymbol{\varepsilon}^{s})^2] \tag{24}$$

with Lamé's first parameter L and the shear modulus G of the AM. Here $\boldsymbol{\varepsilon}^{s}$ the stress-free isotropic volumetric strain induced by Li insertion

$$\boldsymbol{\varepsilon}^{s} = \frac{1}{3}\Omega(c - c_0)\mathbf{I}, \tag{25}$$

where Ω is the molar volume of Li and c_0 the reference concentration.

The stress tensor can be derived from the free energy density as

$$\mathbf{T}_{am} = \frac{\partial \psi_{am}(c, \boldsymbol{\varepsilon})}{\partial \boldsymbol{\varepsilon}} = L\,\mathrm{tr}[\boldsymbol{\varepsilon} - \boldsymbol{\varepsilon}^{s}]\mathbf{I} + 2G\,(\boldsymbol{\varepsilon} - \boldsymbol{\varepsilon}^{s}). \tag{26}$$

The driving force for diffusion is expressed as the gradient of the chemical potential. The partial derivative of the free energy density with respect to the concentration gives the chemical potential

$$\mu = \frac{\partial \psi_{am}}{\partial c} = \mu_0 + RT\left(\ln(c/c_{max}) - \ln\left(1 - c/c_{max}\right)\right) - \Omega T_{H}^{am}, \tag{27}$$

where we have used the hydrostatic stress given by

$$T_{H}^{am} = \frac{1}{3}\,\mathrm{tr}[\mathbf{T}_{am}]. \tag{28}$$

The mass flux is defined as the amount of Li per reference volume flowing with a certain velocity of Li atoms $\vec{v}$

$$\vec{J} = c\ \vec{v} = -cM(c) \cdot \vec{\nabla}\mu, \tag{29}$$

where the gradient of the chemical potential leads to the development of the velocity field. A non-negative definite mobility is chosen according to

$$M\,(c) = \frac{D_0(c_{max} - c)}{RTc_{max}}, \tag{30}$$

which decreases with increasing lattice site occupancy, and in which D_0 is the diffusion coefficient. Combining Eqs. (27), (29) and (30) yields the Li flux

$$\vec{J} = -D_0\vec{\nabla}c + \frac{D_0\Omega c}{RT}(1 - c/c_{max})\vec{\nabla}T_{H}^{am}. \tag{31}$$

The first term on the right hand side of Eq. (31) corresponds to Fickian diffusion that would come from constant mobility and very low concentrations of Li. The second term on the right represents stress gradient driven diffusion, which is negligible at low and high Li concentration.

Finally, based on the balances of mass and linear momentum, respectively, the field equations are given by

$$\dot{c} = -\,\mathrm{div}\,\vec{J} = \mathrm{div}\left(cM\vec{\nabla}\mu\right), \tag{32}$$

$$\mathrm{div}\,\mathbf{T}_{am} = \rho_{am}\frac{\partial^2 \vec{u}}{\partial t^2}, \tag{33}$$

where the term related to the material density of the storage particle ρ_{am} represents dynamic effects resulting from the inertia of the AM.

2.3. Interface

The electrochemical reaction

$$Li^{+} + e^{-} \longleftrightarrow Li \tag{34}$$

takes place at the AM/SE interface, and the reaction rate is qualified by the phenomenological Butler–Volmer equation (Ganser et al., 2019b), which relates the current density i_I to surface overpotential η at the AM/SE interface as

$$i_I = i_0 \left[exp\left((1-\beta)\frac{F\eta}{RT} \right) - exp\left(-\beta \frac{F\eta}{RT} \right) \right], \tag{35}$$

where the damage dependent exchange current density

$$i_0 = i_{00}(1-d)^2 exp\left(\frac{(1-\beta)\mu_{se}}{RT} \right) exp\left(\frac{\beta\mu}{RT} \right) \tag{36}$$

accounts for a direct impact of a crack on the current density by hindering or blocking flow. Here i_{00} is the exchange current density constant with units of A/m^2. The electron-transfer symmetry factor is denoted with β ($\beta = 0.5$). The chemical potential in the SE μ_{se} is assumed to be zero for the single ion conductor ($\mu_{se} = \mu_{0se} = 0$). The surface overpotential η is defined as

$$\eta = \Phi_{am} - \Phi - U, \tag{37}$$

where U is the open circuit potential given by

$$FU = \mu_{se} - \mu. \tag{38}$$

Notice that insertion of Li into the active material takes place at the interface when $\eta < 0$, while extraction of Li from the active material occurs when $\eta > 0$.

The nonlinear nature of the battery behavior makes solution of the system of equations challenging. Therefore, we linearize the Butler–Volmer Eq. (35) as

$$i_I = \frac{i_0 F\eta}{RT}. \tag{39}$$

According to Mykhaylov et al. (2019), the status of this linearized Butler–Volmer equation relies on the relation between the current densities of operation in the battery and the exchange current densities at the interface. This linearized solution is valid except when the current densities of operation are higher than the exchange current densities at the interface. This situation in which the linearized solution is accurate arises since the redox kinetics at the interface will operate at rates that keep them within the linearized regime of the Butler–Volmer equation.

We now combine Eqs. (35)–(39) to obtain the flux of lithium into storage particles at the AM/SE interface as

$$\begin{aligned} J_I &= -\frac{i_I}{F} \\ &= -\frac{i_{00}(1-d)^2 exp\left(\frac{(1-\beta)\mu_{se}}{RT} \right) exp\left(\frac{\beta\mu}{RT} \right) (\Phi_{am} - \Phi - \frac{\mu_{se}-\mu}{F})}{RT}. \end{aligned} \tag{40}$$

It is crucial that through Eqs. (27) and (40) not only Li concentration and electric potential, but also stress and damage variable contribute to the reaction rate.

2.4. Summary of governing equations and boundary conditions

A summary of governing equations for the SE, the interface and the AM, is provided in Table 1. We additionally need a set of initial and boundary conditions, defined on the domain B_{se} describing the SE geometry and its boundary ∂B_{se}. We denote prescribed displacements by $\vec{u}^{\star}$, tractions by $\vec{t}^{\star}$, electric potentials by $\Phi^{\star}$, and current densities by i_p. A well-defined set of boundary conditions is given by $\vec{u} = \vec{u}^{\star}$ on ∂B^{u}_{se} and $\mathbf{T}_{se}\cdot\vec{n} = \vec{t}^{\star}$ on ∂B^{t}_{se} with $\partial B^{u}_{se} \cap \partial B^{t}_{se} = \varnothing$ and $\partial B^{u}_{se} \cup \partial B^{t}_{se} = \partial B_{se}$ for the conservation of linear momentum, $\Phi = \Phi^{\star}$ on ∂B^{Φ}_{se} and $\vec{i}\cdot\vec{n} = i_p$ on ∂B^{i}_{se} with $\partial B^{\Phi}_{se} \cap \partial B^{i}_{se} = \varnothing$ and $\partial B^{\Phi}_{se} \cup \partial B^{i}_{se} = \partial B_{se}$ for the charge balance, as well as $\vec{\nabla} d \cdot \vec{n} = 0$ on ∂B_{se} for the damage variable. The required initial conditions have the form $c(\vec{x}, t_0) = c_0(\vec{x})$, $\vec{u}(\vec{x}, t_0) = \vec{u}_0(\vec{x})$ and $\Phi(\vec{x}, t_0) = \Phi_0(\vec{x})$. The initial crack is introduced as a heterogeneity in the phase field through an initially non-zero history field, which will be specified later.

3. Numerical implementation

We focus on the full 3D spherical particle of radius R_1 embedded in the SE of size R_2 without imposing any symmetry assumptions, as illustrated in Fig. 2. Both the AM and the SE occupy a domain that has a typical volume fraction for cathodes of SSB, such that $R_1/R_2 = 0.7937$ (Deshpande and McMeeking, 2023). The characteristic length scale is defined by $r_0 = 5$ μm, and the characteristic time scale is defined as $t_0 = \frac{r_0^2}{D_0}$. The specific AM and SE under consideration are $LiMn_2O_4$ and $75Li_2S{\cdot}25P_2S_5$ glass, respectively, and the material parameters are summarized in Table 2. According to McGrogan et al. (2017), $Li_2S{\cdot}P_2S_5$ sulfide

Table 1
Summary of governing equations.

	Balance and evolution equations	Constitutive equations and further physical assumption
SE		
Charge	$\operatorname{div}\vec{i}=0$	$\vec{i}=((1-d)^{\alpha}\kappa_0+d^{\alpha}(\beta_1\boldsymbol{D}+\beta_2(\boldsymbol{I}-\boldsymbol{D})\kappa_0))\mathbb{E}$ $\mathbb{E}=-\nabla\boldsymbol{\Phi}$
Elasticity	$\operatorname{div}\mathbf{T}_{se}=\rho_{se}\frac{\partial^2\vec{u}}{\partial t^2}$	$\mathbf{T}_{se}=[(1-d)^2+k]\mathbf{T}_{se}^{+}+\mathbf{T}_{se}^{-}$ $\mathbf{T}_{se}^{\pm}=L_{se}\langle\operatorname{tr}[\boldsymbol{\varepsilon}]\rangle_{\pm}\mathbf{I}+2G_{se}\langle\boldsymbol{\varepsilon}\rangle_{\pm}$
Fracture	$\eta\dot{d}=2(1-d)H_{se}-(\frac{G_c}{l}d-G_c^{se}\ l\ \nabla^2 d)$	$H_{se}=\max_{[0,t]}(\psi_{se}^{+})$ $\psi_{se}^{+}=\frac{L_{se}}{2}\langle\operatorname{tr}[\boldsymbol{\varepsilon}]\rangle_{+}^{2}+G_{se}\operatorname{tr}[\langle\boldsymbol{\varepsilon}\rangle_{+}^{2}]$
Interface		
	$J_I=\frac{i_0\eta}{RT}$	$i_0=i_{00}(1-d)^2 exp\left(\frac{(1-\beta)\mu_{se}}{RT}\right)exp\left(\frac{\beta\mu}{RT}\right)$ $F\eta=F(\boldsymbol{\Phi}_{am}-\boldsymbol{\Phi})-(\mu_{se}-\mu)$
AM		
Diffusion	$\dot{c}=\operatorname{div}\left(cM\vec{\nabla}\mu\right)$	$\mu=\mu_0+RT\left(\ln(c/c_{max})-\ln\left(1-c/c_{max}\right)\right)-\Omega T_H^{am}$ $M(c)=\frac{D_0(1-c/c_{max})}{RT}$
Elasticity	$\operatorname{div}\mathbf{T}_{am}=\rho_{am}\frac{\partial^2\vec{u}}{\partial t^2}$	$\mathbf{T}_{am}=L\operatorname{tr}[\boldsymbol{\varepsilon}-\boldsymbol{\varepsilon}^s]\mathbf{I}+2G(\boldsymbol{\varepsilon}-\boldsymbol{\varepsilon}^s)$ $\boldsymbol{\varepsilon}^s=\frac{1}{3}\Omega(c-c_0)\mathbf{I}$

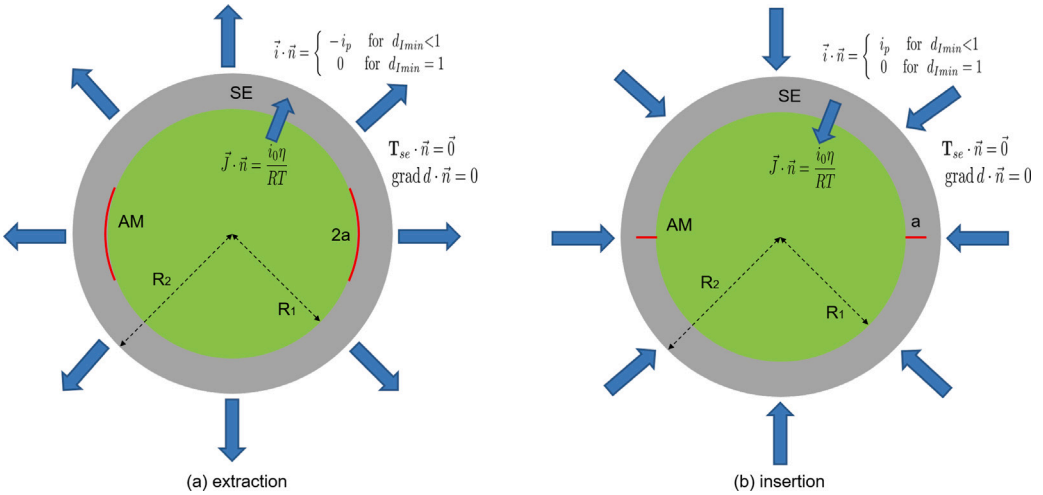

Fig. 2. Geometry and boundary conditions for (a) the Li extraction study and (b) the Li insertion study. The applied current is stopped when $d=1$ everywhere in the interface. The red lines represent the initial crack.

Table 2
Material parameters for the AM ($LiMn_2O_4$) and the SE ($75Li_2S.25P_2S_5$ glass).

Parameters	Description	Values	Ref.
D_0	diffusion coefficient of Li in the AM	7.08×10^{-15} (m^2/s)	Christensen and Newman (2006)
c_{max}	max. concentration of Li in the AM	2.29×10^{4} (mol/m^3)	Zhang et al. (2007)
Ω	partial molar volume of Li in the AM	3.497×10^{-6} (m^3/mol)	Zhang et al. (2007)
E_{am}	Young's modulus of the AM	93 (GPa)	Amanieu et al. (2014)
E_{se}	Young's modulus of the SE	15 (GPa)	Sakuda et al. (2013a)
ν_{am}	Poisson ratio of the AM	0.3	Amanieu et al. (2014)
ν_{se}	Poisson ratio of the SE	0.3	Sakuda et al. (2013a)
ρ_{am}	material density of the AM	4140 (kg/m^3)	Garcıa et al. (2004)
ρ_{se}	material density of the SE	1680 (kg/m^3)	Sakuda et al. (2013a)
κ_0	ionic conductivity in the SE	0.03 (S/m)	Sakuda et al. (2013a)
G_c	critical energy release rate of the SE	1 (J/m^2)	
i_{00}	exchange current density constant	30 (A/m^2)	
T	temperature	298.15 (K)	
R	gas constant	8.3145 J/(mol.K)	

electrolytes demonstrate low resistance to fracture in the range of 1–3 J/m^2. Here, a typical value of 1 J/m^2 for $75Li_2S{\cdot}25P_2S_5$ glass is assumed, which is in the range of experimental results for this material (McGrogan et al., 2017). "State of charge" (SOC), also called the average concentration, is defined as $SOC = \int_{B_{am}} c/c_{max} dV/V$. The current density $\vec{i}$ is normalized as $\bar{\vec{i}} = \vec{i} r_0/c_{max} D_0 F$.

For Li extraction, the largest tensile stress occurs at the interface, such that delamination could happen. An initial crack is therefore introduced at the middle of the interface with cylindrical shape with height $2a$, as shown in Fig. 2a. We prescribe this initial crack through the damage variable by defining an initially non-zero history field of the form

$$H_0^{ex} = \alpha_H e^{-((\sqrt{x^2+y^2+z^2}-R_1)/\beta_H)^2} \times \begin{cases} 1 & s^{ex} < 0 \\ e^{-(s^{ex}/\beta_H)^2} & s^{ex} \geq 0, \end{cases} \tag{41}$$

where $\alpha_H = 10^5$ and $\beta_H = l/10$. The damage variable is allowed to relax in a number of iterations to the given history field. The local distance to the crack tip is defined by

$$s^{ex} = R_1 \arcsin \frac{|z|}{R_1} - a. \tag{42}$$

It should be mentioned that the definition of this initially non-zero history field is the key way to ensure crack growth along the interface during extraction and to induce lower effective fracture toughness of the interface. For Li insertion, an initial radial crack is introduced in the SE adjacent to the interface with the shape of a ring with length a, see Fig. 2b. It is prescribed through an initially non-zero history field, as given by

$$H_0^{in} = \alpha_H e^{-(z/\beta_H)^2} \times \begin{cases} 1 & s^{in} < 0 \\ e^{-(s^{in}/\beta_H)^2} & s^{in} \geq 0, \end{cases} \tag{43}$$

where the local distance to the crack tip is given by

$$s^{in} = |\sqrt{x^2 + y^2} - R_1| - a. \tag{44}$$

Since the mechanically coupled diffusion Eq. (32) involves third-order spatial derivatives in displacement, the standard finite element method with C^0-continuous Lagrange basis functions is not sufficient for discretization. To overcome this numerical difficulty, we introduce the chemical potential as an additional degree of freedom to split this third order partial differential equation into two second-order equations. The AM system is described by the three Eqs. (27), (32) and (33) with the independent variables c, μ and $\vec{u}$, respectively. The SE system is described by the three Eqs. (6), (16) and (19) with the independent variables Φ, d and $\vec{u}$, respectively. The above two systems couple with each other through the interfacial reaction (40) at the interface, in which concentration, electric potential, displacement, and damage variable evolve simultaneously. The resulting set of equations is first written in weak form (see Appendix A), and then implemented in the finite-element, multiphysics framework MOOSE (Gaston et al., 2009).

The system of nonlinear equations is solved using the preconditioned Jacobian Free Newton Krylov (PJFNK) method with a generalized minimal residual method (GMRES) Krylov iterative solver (Gaston et al., 2009), so that there is no need to form the explicit tangent matrix, thereby saving computational time and storage space. The fully coupled system is solved using the Additive Schwarz method (ASM) preconditioner with a LU subsolver (Gaston et al., 2009), which is found in our experience to work well. The implicit Backward-Euler time integration method is employed for time integration in the diffusion equation. The Newmark method (Newmark, 1959) is used for time integration in the equations describing the balance of linear momentum. To prevent arbitrary rigid body displacements and rotations, the six 3D rigid body modes are removed at the solver level, which, in our experience, is found to provide better convergence compared to methods involving pinning the displacement at certain vertices. An adaptive time stepping method is employed to both find a good time step for the relatively smooth diffusion process and to adjust quickly to the initiation of unstable crack growth. In all the simulations, the length scale parameter is set to $l/R_2 = 0.05$. In this way, the range of transition between cracked and uncracked state is sufficiently small in comparison to the size of the crack. To resolve the damage field in a sufficiently precise way, the mesh element size is chosen to be less than $l/2$ (Miehe et al., 2010). The mesh in our simulations reaches up to 2.35 million in terms of number of elements. Simulations are performed on a high-performance Linux computer cluster. 3-D simulations are run on 896 processors and take up to a maximum of 18 days.

4. Results and discussion

In this section, before addressing delamination and SE cracking, we carry out validation of the proposed model by comparing the numerical results against the analytical solution for a 2D cylindrical particle embedded in the SE. Then we focus on the 3D spherical storage particle embedded in the SE to study interface delamination during extraction as well as SE cracking during insertion.

4.1. Numerical validation

For the sake of validation, especially the connection between the AM and the SE through interfacial reaction at the interface, we exclude the mechanics to study the electro-chemical response in a 2D cylindrical particle embedded in the SE during insertion,

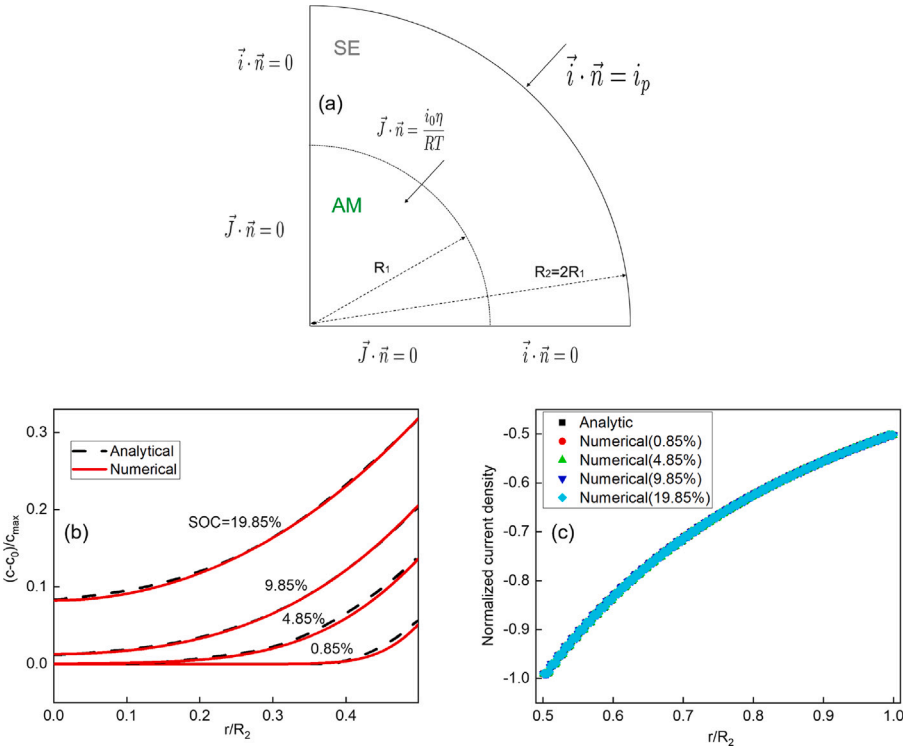

Fig. 3. (a) Geometry and boundary conditions for a 2D cylindrical particle embedded in SE during insertion. (b) Normalized concentration $(c-c_0)/c_{max}$ vs normalized radial coordinate r/R_2 for different SOC during insertion; (c) Normalized current density vs normalized radial coordinate r/R_2 for different SOC during insertion: comparison of numerical simulation and analytical solution.

see Fig. 3a. The imposed current density at the SE surface is fixed to achieve a galvanostatic discharging operation. The electric potential in the AM, Φ_{am}, is set to zero. The analytical solution for Li concentration in the AM is given by Crank (1979)

$$c-c_0=-\frac{J_I R_1}{D_0}\left(\frac{2D_0 t}{R_1^2}+\frac{r^2}{2R_1^2}-0.25-2\sum_{n=1}^{\infty} exp(-D_0\alpha_n^2 t/R_1^2)\frac{J_0(r\alpha_n/R_1)}{\alpha_n^2 J_0(\alpha_n)}\right), \tag{45}$$

where α_n are the positive roots of Bessel functions $J_1(\alpha)=0$. In the SE, the analytical solution for the current density magnitude is derived as

$$i_r=i_p\frac{R_2}{r}. \tag{46}$$

The distribution of Li concentration in the AM and current density in the SE is provided in Fig. 3b and c. We find that the concentration profiles obtained from the numerical simulation and the analytical solution match each other at different SOC. As shown in Fig. 3c, the current density in the SE is always the same for different SOC in the AM due to the galvanostatic discharging operation. Also, the plots of current density magnitude from the numerical simulation are consistent with the analytical solution. Therefore, the proposed finite element simulation is validated with the analytical solution.

4.2. 3D spherical storage particles embedded in the solid electrolyte during extraction

Here, the fully coupled system of Li diffusion, ionic conduction, electrochemical reaction, mechanical stress and fracture is investigated for a 3D storage particle surrounded by SE. The simultaneous study of all these physical processes reveals interesting phenomena, which are examined in the following. Since an initial crack is introduced at the interface to study interface delamination without crack growth inside the SE during extraction, $\alpha=0$ and $\beta_1=\beta_2=0$ are therefore taken into account in Eq. (4). This means hindering and blocking of extraction flow at the interface is implemented through the behavior of d in Eq. (40). It should be noticed that, in the presence of interfacial defects, the Li extraction process is not uniformly galvanostatic but is controlled by the charge balance in the whole surface of SE.

The SE sizes are chosen as $R_2=5$ μm, 10 μm and 20 μm, the crack sizes are $a=0.000125$ μm, 0.00125 μm, 0.0125 μm, 1.25 μm, 2.50 μm and 4.98 μm and the applied current density is given values of $i_p=0.5$ A/m^2, 2 A/m^2, 10 A/m^2 and 20 A/m^2. As shown in Table 3, a number of different delamination phenomena occur, depending the combination of parameters chosen. The simulations are started with maximum concentration, i.e., $c_0/c_{max}=0.95$, and stopped when the storage particle completely detaches from the

Table 3
Input parameters, i.e., SE size R_2, crack length a and applied current density i_p, as well as the occurrence of the different delamination phenomena in the extraction study. Here t_{ck} and SOC_{ck}, respectively, represent the time and SOC when crack growth is initiated. C represents the initial C-rate based on the initial applied current.

Parameters				Delamination behavior					
$R_2[\mu m]$	$a[\mu m]$	$i_p[A/m^2]$	C	unstable	add. cracks	homogeneous	complete	$t_{ck}(h)$	SOC_{ck}
5	0.000125	10	19.55	yes	no	no	yes	0.043	0.53
5	1.25	2	2.68	yes	no	no	yes	2.10	0.63
5	1.25	10	13.39	yes	no	no	yes	0.28	0.64
5	1.25	20	26.79	yes	no	no	yes	0.13	0.64
10	0.0125	20	19.52	yes	no	yes	yes	0.038	0.67
10	1.25	2	1.65	yes	no	no	yes	1.48	0.69
10	1.25	10	8.24	yes	no	no	yes	0.26	0.69
10	1.25	20	16.47	yes	no	no	yes	0.09	0.71
10	2.50	2	1.34	yes	no	no	yes	3.57	0.73
10	2.50	10	6.70	yes	no	no	yes	0.69	0.73
10	2.50	20	13.39	yes	yes	no	yes	0.27	0.74
20	0.00125	20	9.78	yes	no	yes	yes	0.076	0.77
20	0.0125	20	9.77	yes	no	yes	yes	0.077	0.77
20	1.25	2	0.90	yes	no	no	yes	1.32	0.76
20	1.25	10	4.50	yes	yes	no	yes	0.20	0.78
20	1.25	20	9.01	yes	yes	no	yes	0.09	0.80
20	4.98	0.5	0.17	yes	no	no	yes	55.94	0.79
20	4.98	2	0.67	yes	no	no	yes	8.58	0.79
20	4.98	10	3.35	yes	yes	no	yes	1.11	0.80
20	4.98	20	6.71	yes	yes	no	yes	0.32	0.83

SE. To present these in a comprehensible way, we begin with the case of a small SE size (i.e., a small particle size due to the fixed ratio R_1/R_2) and then go through the several possibilities of delamination step by step.

4.2.1. Unstable interface delamination

To study the interplay of Li diffusion, ionic conduction, interfacial reaction and mechanical stress during delamination, we investigate the parameter combination $R_2 = 5$ μm, $a = 1.25$ μm and $i_p = 10$ A/m^2. The physical behavior discussed in the following is representative of all input parameters that neither lead to the creation of additional cracks nor to homogeneous interface delamination.

As the current flows out of the SE at its perimeter, Li will be extracted from the storage particle via interfacial reaction. During Li extraction from the AM, Li concentration reduces in it and the storage particle shrinks. Due to a direct impact of the interfacial defect on the Li flux, this shrinkage is most pronounced close to the intact part of the interface, where the largest amount of Li is being extracted. Because of the inhomogeneous volume shrinkage and the constraint of the SE, tensile stress develops at the intact part of the interface and compressive stress is generated in the interior of the storage particle as well as in the SE in the circumferential direction, see Fig. 4d. The role of the concentration difference on the generation of mechanical stress can be observed by comparing the maximum concentration difference in Fig. 5a with the highest value anywhere of the maximum principal stress in Fig. 5b. It is observed that the stress rises with the maximum concentration difference. Along the crack surfaces there is almost no stress at all. It is expected that the mechanical driving force for diffusion, given in Eq. (31), should aid Li transport towards the crack tips, and away from the crack faces. But Li concentration is much higher at the crack faces than at the intact segment of the interface, see $SOC = 71\%(t/t_0 = 0.24)$ in Fig. 4c. This interesting behavior is induced by the fact that stress assisted diffusion competes with the direct blocking of the Li flux by the interfacial crack. As a consequence, there is higher concentration at the interface region where the initial crack is located. Similarly, a higher current density is generated at the cracked interface region, see Fig. 4e. Presumably the current density at the initial crack is parallel to the crack and is not through it.

When SOC approaches 0.64 ($t/t_0 = 0.29$), the stress at the crack tip becomes large enough to initiate delamination. The initial crack starts to propagate along the interface in an unstable way on a time scale much smaller by orders of magnitude than those associated with the Li diffusion process in the storage particle and the ionic conduction in the SE. This is shown by a step-like behavior of the graph of crack length versus time plotted in Fig. 5d. The appearance of unstable delamination is likely due to the fact that the crack grows into a high tensile stress field at the intact part of the interface that is constrained by the SE. Due to the small time scale of the unstable delamination, the Li distribution does not adjust simultaneously with the damage field. Thus the Li concentration is essentially frozen during the delamination process. Similarly, the current density is also unchanged during the unstable delamination process.

As illustrated in Fig. 5c, unstable delamination is associated with the peak of the stress curve. After this peak, the maximum principal stress drops rapidly to a value of $max\ \sigma_I = 0.8$ GPa. We attribute this dramatic drop to the reduced constraint of the SE as a consequence of unstable delamination. The volume shrinkage of the storage particle is less restricted by the smaller remaining interface ligament, and the stress field then relaxes on a very short time scale controlled by the unstable delamination, leading to the dramatic drop in the maximum stress. During the unstable delamination process, the bottom part of the interface is first detached

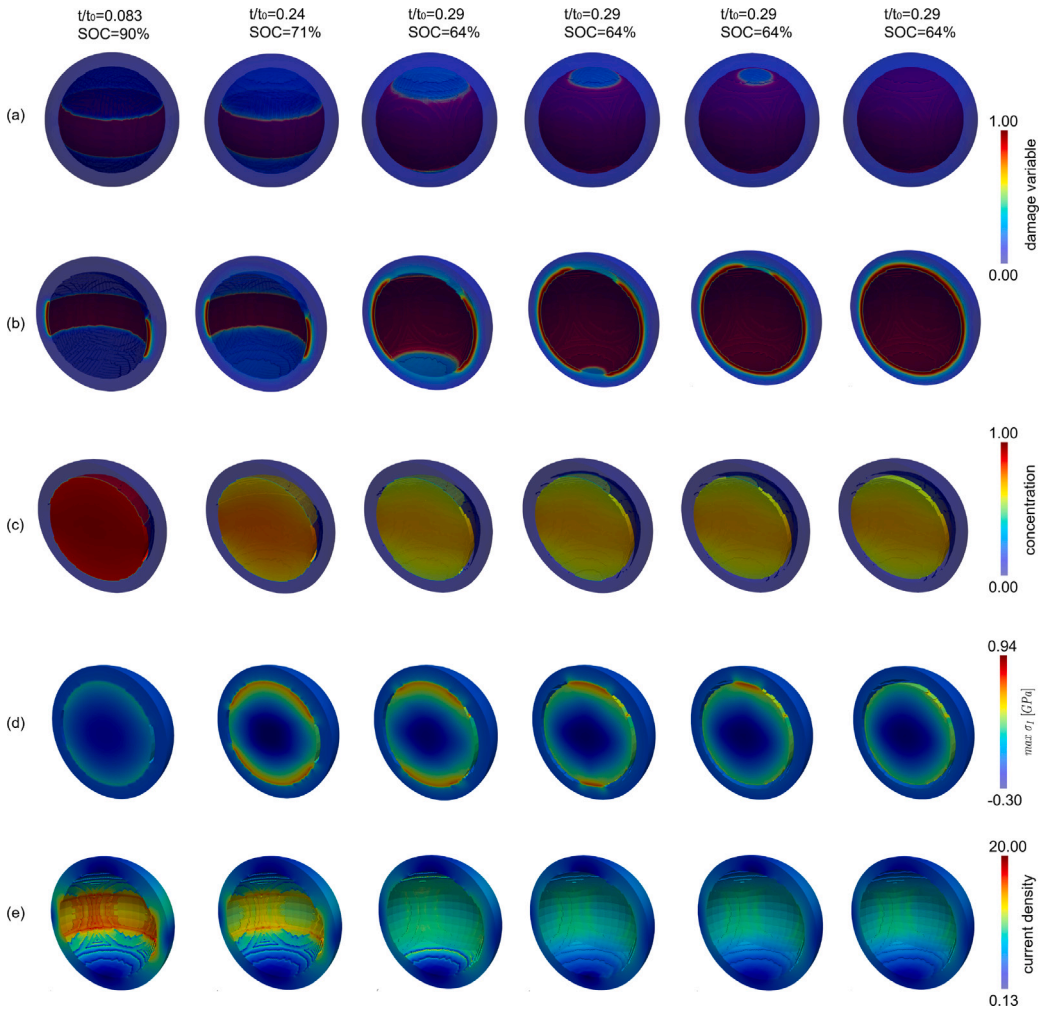

Fig. 4. (a) Damage variable d, (b) Damage variable d (only a half of the 3D spherical storage particle embedded in the SE), (c) normalized concentration c/c_{max}, (d) the maximum principal stress σ_I and (e) normalized current density during Li extraction in a 3D spherical storage particle embedded in SE with $R_2 = 5$ μm, $a = 1.25$ μm and $i_p = 10$ A/m^2. For better visibility, only a half of the 3D spherical storage particle embedded in the SE is shown in (b–e), and only a half of the SE is shown in (e). Regions with $d > 0.95$ are removed in (c–e) to show the location of the crack, and iso-surface visualization is used in (a–c).

followed by the top one, although the initial crack is introduced at the middle of the interface. This symmetry breaking phenomenon is probably induced by numerical round-off and truncation.

As shown in Table 3, interface delamination takes place for all input parameters. In order to explain the appearance of delamination, we perform the following analytic assessments. The equations used hereby are based on very simplified assumptions and shall only serve for a qualitative understanding of the delamination.

For an estimate, we neglect the influences of Li in the storage particle on the stress field near the crack tip and the free energy of the system via its chemical potential. The separation of the interface between the AM and the SE is assumed to be negligible. According to Deshpande and McMeeking (2023), the stress in the storage particle is hydrostatic, given by

$$T_{am} = -\frac{\frac{2\varepsilon^s}{3}(1-f)E_{se}}{(1+\nu_{se}) + 2(1-2\nu_{se})f + 2(1-2\nu_{am})(1-f)\frac{E_{se}}{E_{am}}}, \tag{47}$$

where f is the volume fraction of AM.

A mode I crack tip stress field is assumed for the crack in the interface with stress intensity factor given by Tada (2000)

$$K_I = \frac{2}{\pi} T_{am}\sqrt{\pi a}, \tag{48}$$

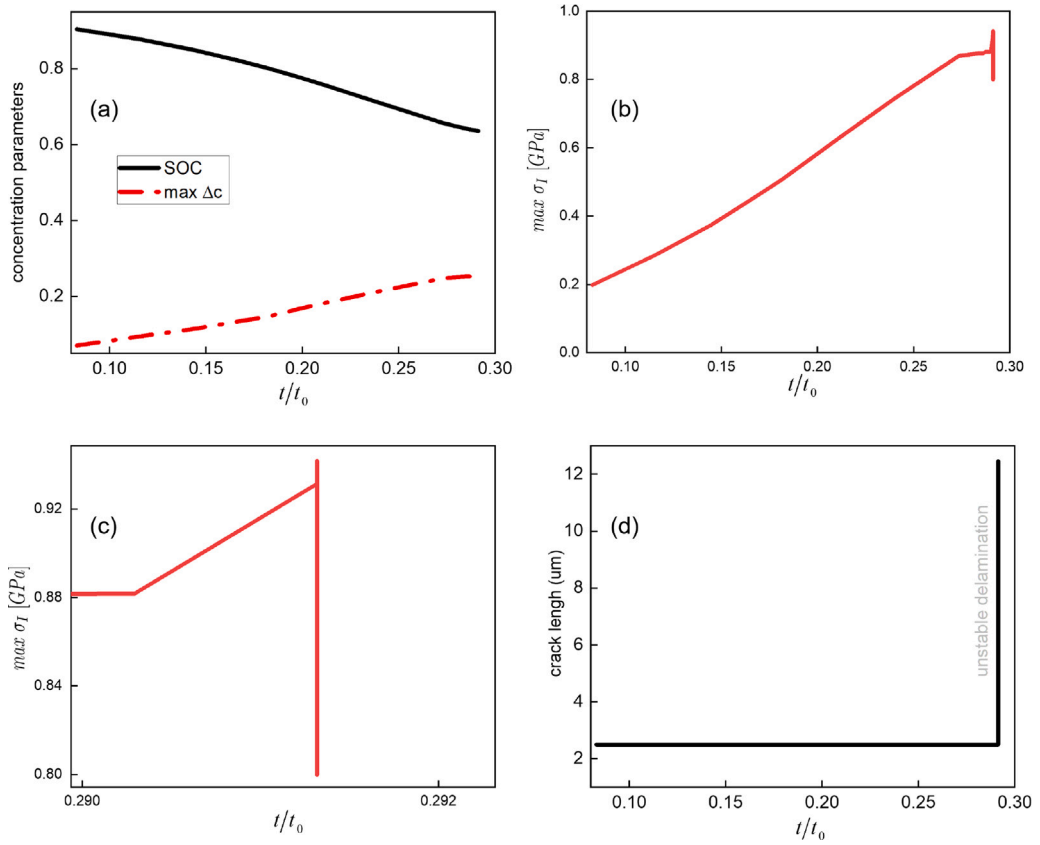

Fig. 5. Characteristic results for Li extraction with $R_2 = 5$ μm, $a = 1.25$ μm and $i_p = 10$ A/m^2 as a function of time. (a) SOC and maximum concentration difference $max\ \triangle c$ in units of maximum concentration c_{max}. (b) The highest value of the maximum principal stress $max\ \sigma_I$. (c) Magnified view of the highest value of the maximum principal stress $max\ \sigma_I$. (d) Crack length.

which is assumed not to be influenced by the presence of lithium adjacent to the crack. The energy release rate related to the stress intensity factor is (Rice, 1988; Deshpande and McMeeking, 2023)

$$G = \left(\frac{1-\nu_{am}^2}{E_{am}} + \frac{1-\nu_{se}^2}{E_{se}}\right)\frac{K_I^2}{2}. \tag{49}$$

To predict crack growth we set the energy release rate equal to the critical energy release rate, G_c, and combine Eq. (49) with Eqs. (47) and (48) to predict the critical shrinkage strain to delaminate the interface as

$$\epsilon_T^s = -\frac{3[(1+\nu_{se})E_{am} + 2(1-2\nu_{se})fE_{am} + 2(1-2\nu_{am})(1-f)E_{se}]}{2(1-f)E_{am}E_{se}} \cdot \sqrt{\frac{\pi G_c}{2d\left(\frac{1-\nu_{am}^2}{E_{am}} + \frac{1-\nu_{se}^2}{E_{se}}\right)}}. \tag{50}$$

We apply the material parameters for $LiMn_2O_4$ and $75Li_2S{\cdot}25P_2S_5$ glass in Table 2 into Eq. (50) with $f = 0.5$. Then the critical volume shrinkage to propagate the crack will be approximately 4.72%. Therefore, the volume shrinkage of 7.3% (Hunter, 1981) for $LiMn_2O_4$ is obviously higher than the critical volume shrinkage, such that it is very likely interface delamination to be associated with shrinkage of $LiMn_2O_4$. As s result, all input parameters in Table 3 lead to complete interface delamination.

4.2.2. Additional cracks

In our simulations with larger SE sizes (i.e., larger particle sizes due to the fixed ratio R_1/R_2) and higher applied current densities, additional cracks are nucleated at locations, where there are no initial cracks. This effect is observed for $R_2 \geq 10$ μm, $a \geq 1.25$ μm and $i_p \geq 10$ A/m^2, as shown in Table 3. An example of the resulting delamination evolution is given in Fig. 6 with $R_2 = 20$ μm, $a = 4.98$ μm and $i_p = 10$ A/m^2.

As seen in Fig. 6, once SOC approaches 80% ($t/t_0 = 1.13$), not only the initial crack starts to growth, but also additional cracks from the top and bottom of the interface are nucleated. The additional cracks propagate faster and the storage particle detaches

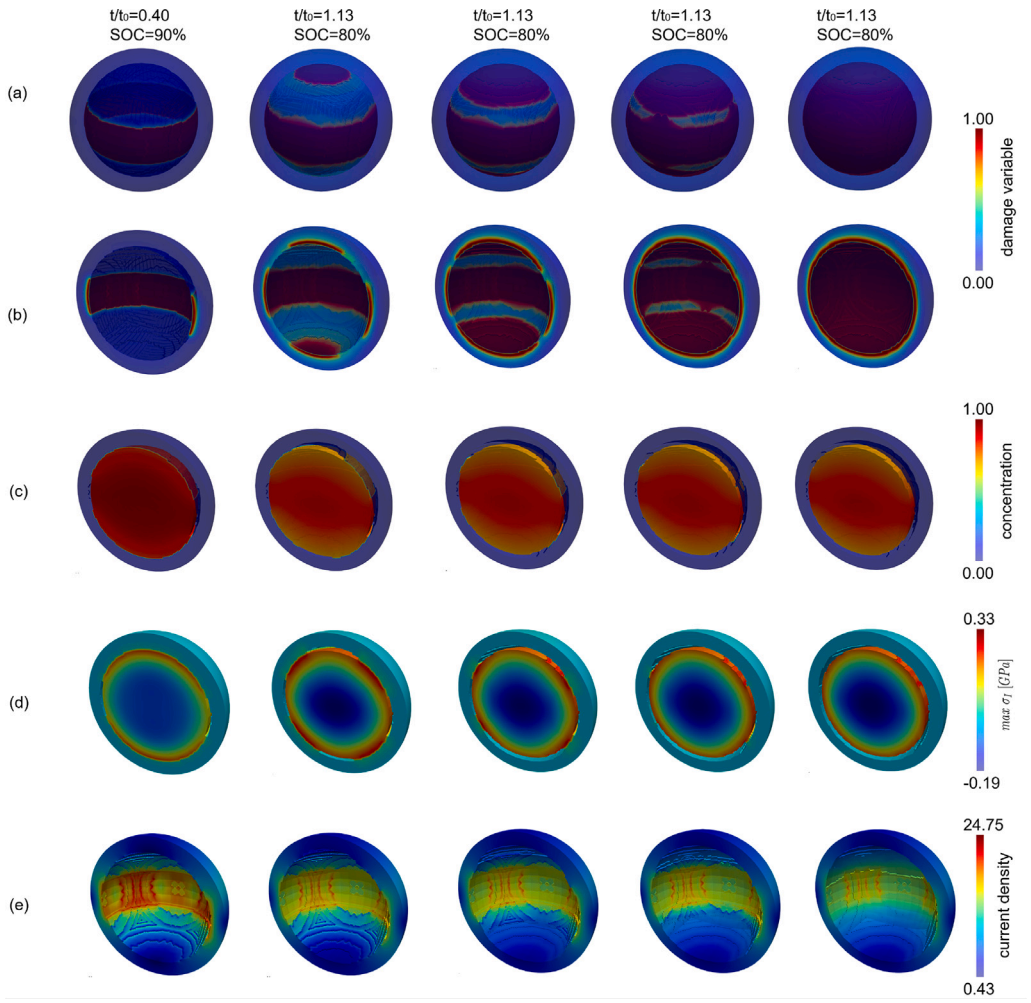

Fig. 6. (a) Damage variable d, (b) Damage variable d (only a half of the 3D spherical storage particle embedded in the SE), (c) normalized concentration c/c_{max}, (d) the maximum principal stress σ_I and (e) normalized current density during Li extraction in a 3D spherical storage particle embedded in SE with $R_2 = 20$ µm, $a = 4.98$ µm and $i_p = 10$ A/m^2. For better visibility, only a half of the 3D spherical storage particle embedded in the SE is shown in (b–e), and only a half of SE is shown in (e). Regions with $d > 0.95$ are removed in (c–e) to show the location of the crack, and iso-surface visualization is used in (a–c).

completely from the SE abruptly. The behavior of Li diffusion and ionic conduction resemble those described before. Both do not adapt to the modified damage field during the unstable delamination process due to the short period of time involved. The additional cracks come from the smooth approximation of the discrete cracks inherent in the phase field method. Although the stress can be relaxed by growth of the initial crack, a high stress level still exists on the remote perimeter of the interface where the damage variable is initially zero, leading to the creation of additional cracks. The length scale parameter l thus acts as a material parameter, and defines an effective initial crack length. Please see the more detailed discussion on the role of the length scale parameter as an effective material parameter in Klinsmann et al. (2015a). However, it is doubtful whether the initial crack length for defects modeled in such a manner can be obtained from a specified value of l in a precise way. Hence, the meaning of the results of the corresponding computations cannot be deduced in the same way as in simulations where the initial crack size is introduced in a well-controlled way.

4.2.3. Homogeneous interface delamination

In order to examine whether or not homogeneous interface delamination can appear, we decrease the defect size to produce interfaces containing very small defects such that the interface is in the defect insensitive regime. We find that the situation above with higher applied current densities and larger SE sizes makes homogeneous delamination possible, see Table 3. We study the parameter combination with $R_2 = 20$ µm, $a = 0.00125$ µm and $i_p = 20$ A/m^2. With respect to the phenomena observed, the set of parameters is similar to the same combination with $a = 0.0125$ µm, as well as the parameter combination with $R_2 = 10$ µm, $a = 0.0125$ µm and $i_p = 20$ A/m^2.

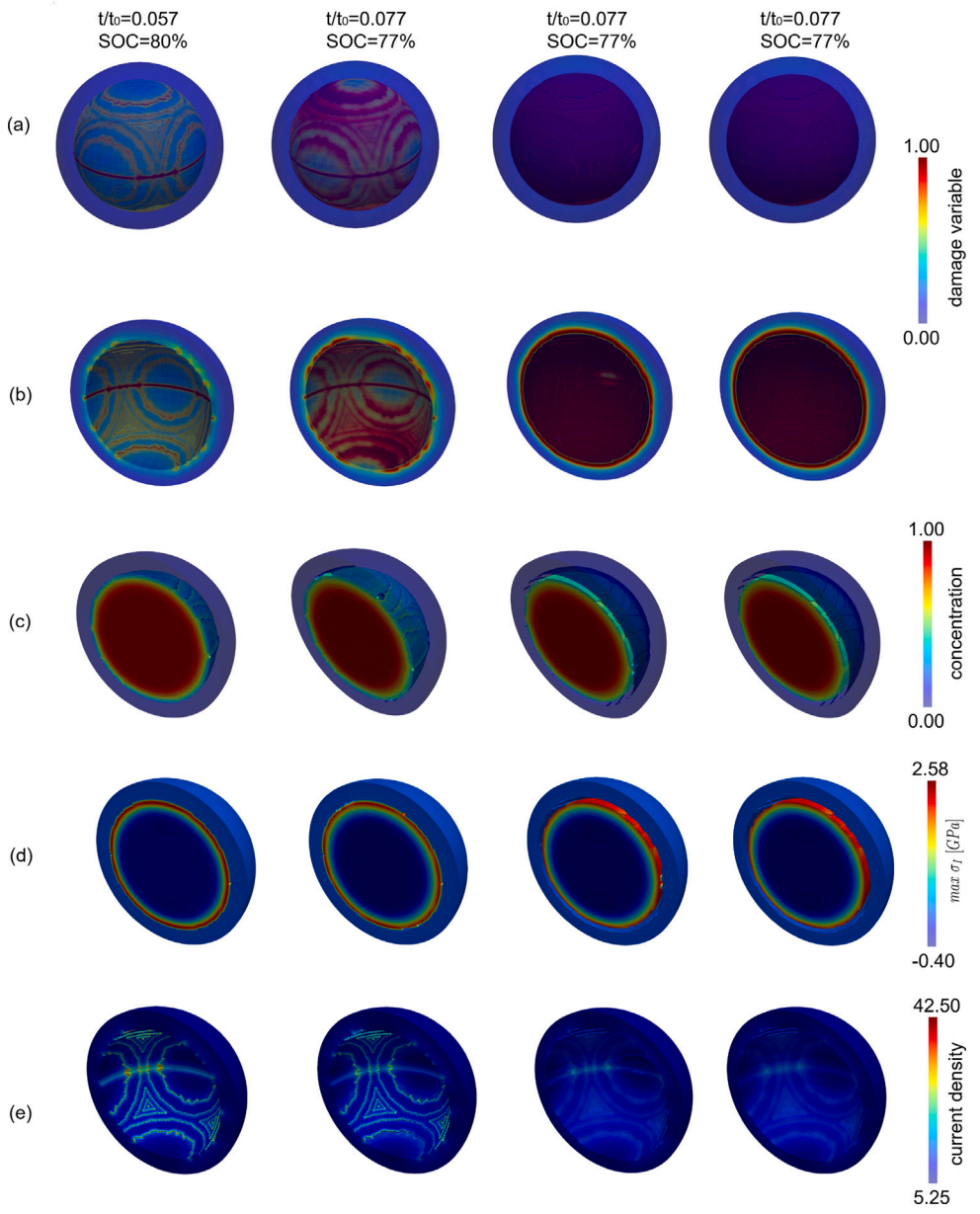

Fig. 7. (a) Damage variable d, (b) Damage variable d (only a half of the 3D spherical storage particle embedded in the SE), (c) normalized concentration c/c_{max}, (d) the maximum principal stress σ_I and (e) normalized current density during Li extraction in a 3D spherical storage particle embedded in the SE with $R_2 = 20$ μm, $a = 0.00125$ μm and $i_p = 20$ A/m^2. For better visibility, only a half of the 3D spherical storage particle embedded in the SE is shown in (b–e), and only a half of SE is shown in (e). Regions with $d > 0.95$ are removed in (c–e) to show the location of the crack, and iso-surface visualization is used in (a–c).

As a result of the smaller defect size, the whole interface delaminates simultaneously, as shown in Fig. 7. The delamination process again takes place on a time scale short enough so that both the Li concentration distribution and the current density are barely able to adapt to the damage field. The reason for homogeneous interface delamination lies in a very high tensile stress distribution at the interface. To illustrate this point, the graphs of SOC, the maximum concentration difference and stress for the cases with initial crack length $a = 0.00125$ μm and $a = 4.98$ μm (the fraction of delaminated interface is 0.2) are plotted in Fig. 8. It takes a much shorter time to initiate delamination for the smaller initial crack length, though the same current density $i_p = 20$ A/m^2 is applied. This is due to the fact that for the smaller initial crack length, less current is shared by the cracked face next to the SE, and more Li is extracted from the intact part of the interface due to the charge balance in the whole surface of SE. As a result, a smaller interfacial defect leads to a larger extraction rate for the storage particle, and more Li is extracted through the interface, leading to a much larger maximum concentration difference in Fig. 8a. Thus much higher tensile stresses are induced nearly in the whole region of the interface due to a smaller defect length, see Figs. 7d and 8b. The highest value of the maximum principal stress

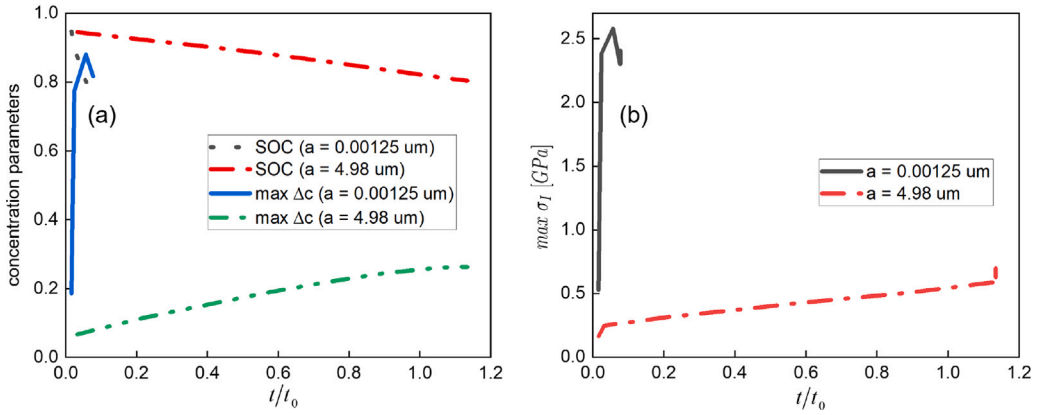

Fig. 8. Characteristic results for Li extraction with $R_2 = 20$ μm, $i_p = 20$ A/m^2 and $a = 0.00125$ μm or $a = 4.98$ μm as a function of time. (a) SOC and maximum concentration difference $max\ \triangle c$ in units of maximum concentration c_{max}. (b) The highest value of the maximum principal stress $max\ \sigma_1$.

Table 4
Input parameters, i.e., SE size R_2, crack length a and applied current density i_p, as well as the occurrence of the different crack behavior in the insertion study. Here t_{ck} and SOC_{ck}, respectively, represent the time and SOC when crack growth is initiated. C represents the initial C-rate based on the initial applied current.

Parameters				Crack behavior						
$R_2[\mu m]$	$a[\mu m]$	$i_p[A/m^2]$	C	branching	breakage	add. cracks	stable delamination	Nr. of SE segments	$t_{ck}(h)$	SOC_{ck}
5	0.21	2	3.91	yes	yes	yes	partial	10	0.24	0.39
5	0.21	10	19.55	yes	yes	yes	partial	10	0.04	0.43
5	0.21	20	39.10	yes	yes	yes	partial	12	0.022	0.43
20	0.21	2	0.98	yes	yes	yes	complete	12	0.43	0.24
20	0.21	10	4.89	yes	yes	yes	complete	18	0.12	0.23
20	0.21	20	9.78	yes	yes	yes	complete	21	0.07	0.21

for the smaller initial crack length is about 3.5 times that for the larger initial crack length. Hence, higher tensile stresses distributed at the interface are able to trigger homogeneous interface delamination for a smaller initial crack length. This behavior is consistent with the concept that the smaller crack size is chosen to be in the defect insensitive regime as far as delamination is concerned.

As expected, the onset time of delamination is reduced for higher applied current densities i_p and larger SE sizes R_2, see Table 3. However, the onset of delamination is delayed for a larger initial crack length. As mentioned before, this is related to damage dependent interfacial reaction that a larger interfacial defect leads to a lower total rate of Li extraction due to the charge balance in the whole surface of SE. On the other hand, more particle storage capacity can be utilized for smaller SE sizes R_2 and smaller initial crack lengths a prior to delamination. For example, as shown in Table 3, when $a = 1.25$ μm and $i_p = 20$ A/m^2, 16% more particle storage capacity is utilized for $R_2 = 5$ μm than $R_2 = 20$ μm (see the difference in SOC_{ck}). As for the smaller initial crack length $a = 0.000125$ μm, 11% more particle storage capacity is utilized compared to $a = 1.25$ μm when $R_2 = 5$ μm and $i_p = 10$ A/m^2. Interestingly, the applied current density has little effect on the utilization of particle storage capacity.

4.3. 3D spherical storage particles embedded in the solid electrolyte during insertion

We now focus on the opposite charging condition and examine the behavior of SE cracking for the 3D spherical storage particle embedded in the SE during insertion. Since an arbitrarily located crack in the interior of the SE may hamper ionic or electronic conduction perpendicular to the crack faces in a significant way, $\alpha = 2$ and $\beta_1 = 0$ are taken into account in Eq. (4). We here assume ionic or electronic conduction parallel to the crack faces is also hindered by the crack via $\beta_2 = 0$. This may not describe the actual physical situation perfectly, but nevertheless provides a good first approximation in absence of physically sound information on the precise ionic conduction conditions parallel to the crack faces.

The SE sizes are chosen as $R_2 = 5$ μm and 20 μm, the crack size is $a = 0.21$ μm, and the applied current density is given values of $i_p = 2$ A/m^2, 10 A/m^2 and 20 A/m^2. As shown in Table 4, the crack not only branches but also breaks the SE into parts for all input parameters during Li insertion. The simulations are started with minimum concentration, i.e. $c_0/c_{max} = 0.05$, and stopped when the SE breaks into several parts. We begin with the case with a small SE size and a low applied current density and then go through several possibilities of cracking behavior step by step.

4.3.1. Electrolyte breakage and crack branching

To study the interplay of Li diffusion, current density, interfacial reaction, and mechanical stress during crack growth, we first investigate the parameter combination $R_2 = 5$ μm, $a = 0.21$ μm and $i_p = 2$ A/m^2. With respect to the phenomena observed in

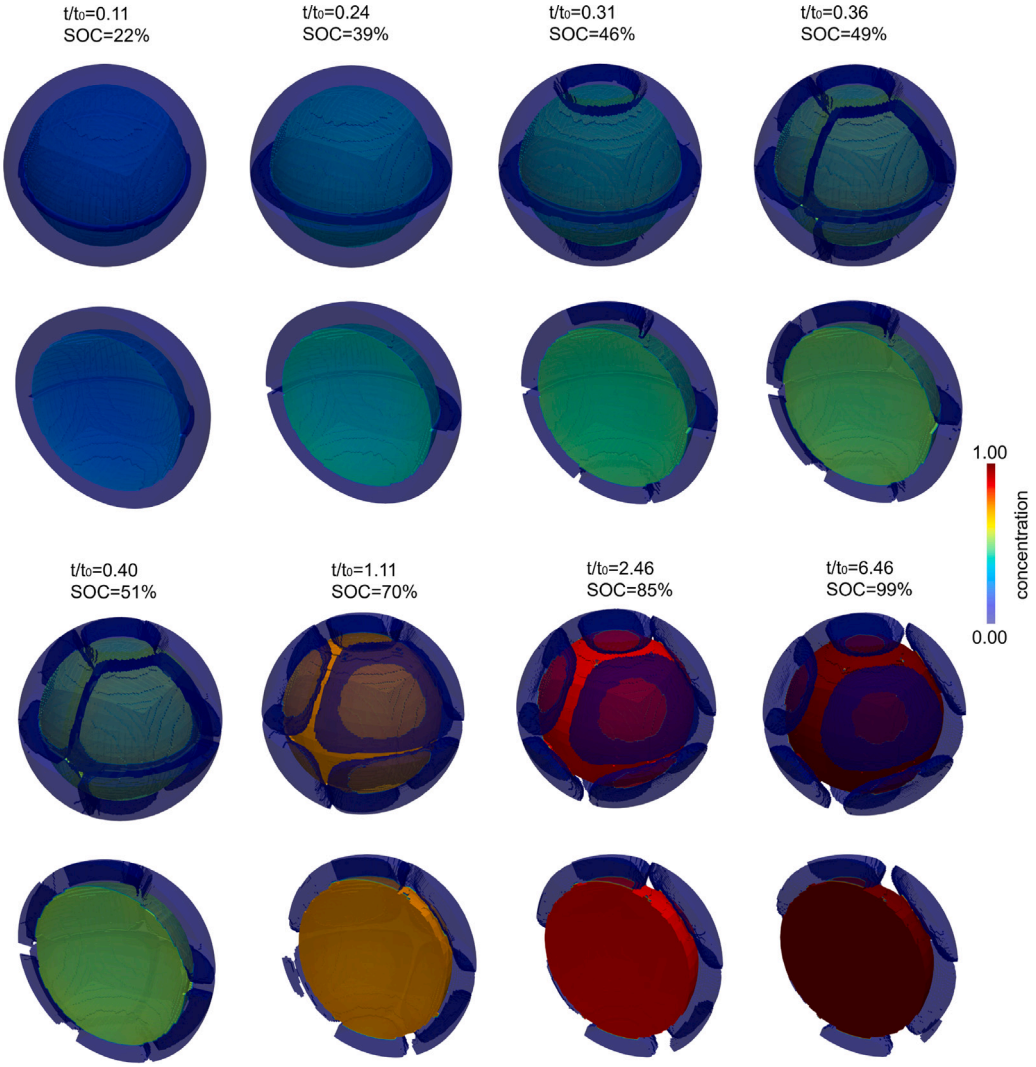

Fig. 9. Normalized concentration c/c_{max} during Li insertion in a 3D spherical storage particle embedded in the SE with $R_2 = 5$ μm, $a = 0.21$ μm and $i_p = 2$ A/m^2. For better visibility, only a half of the 3D spherical storage particle embedded in the SE is shown in the second and fourth rows. Regions with $d > 0.95$ are removed to show the location of the crack, and iso-surface visualization is used for better visibility.

Figs. 9–13, the set of parameters is similar to the parameter combination with $R_2 = 5$ μm, $a = 0.21$ μm and $i_p = 10$ A/m^2, as well as the parameter combination with $R_2 = 5$ μm, $a = 0.21$ μm and $i_p = 20$ A/m^2.

As the ionic current flows into the SE at its perimeter, Li will be inserted into the storage particle via interfacial reaction. During Li insertion, the Li concentration in the AM increases and the storage particle expands. This expansion is most pronounced at the interface, where the largest amount of Li is being inserted. Because of the inhomogeneous volume expansion and the constraint of the SE, compressive stress develops at the interface and tensile stress is generated in the interior of the storage particle as well as in the SE in the circumferential direction, see Figs. 9 and 10.

When SOC approaches 39% ($t/t_0 = 0.24$), the stress at the crack tip becomes large enough to initiate crack growth. The initial crack penetrates all the way through to the perimeter of the SE and breaks it into two, see Fig. 11. We emphasize that this happens in only in one half cycle of lithiation. Such unstable crack growth behavior is due to the fact that the crack will grow into a rising stress field as shown in Fig. 10. The breakage process takes place on a time scale short enough so that both the Li concentration distribution in the storage particle and the current density in the SE are essentially fixed. As shown in Fig. 13d, unstable crack growth is associated with the first peak, of the stress curve, denoted by A. Immediately after this peak, the highest value anywhere of the maximum principal stress drops rapidly. This dramatic drop is due to inertia driven crack propagation in the last stages of growth (Klinsmann et al., 2016b). When the crack abruptly propagates, momentum is built up in the material adjacent to the upper and lower crack faces. The inertia induced stress, which is caused by the deceleration of the material, tends to cause continued crack growth when crack growth is slowed down by crack tip compressive stresses or other causes. This inertia induced stress then relaxes

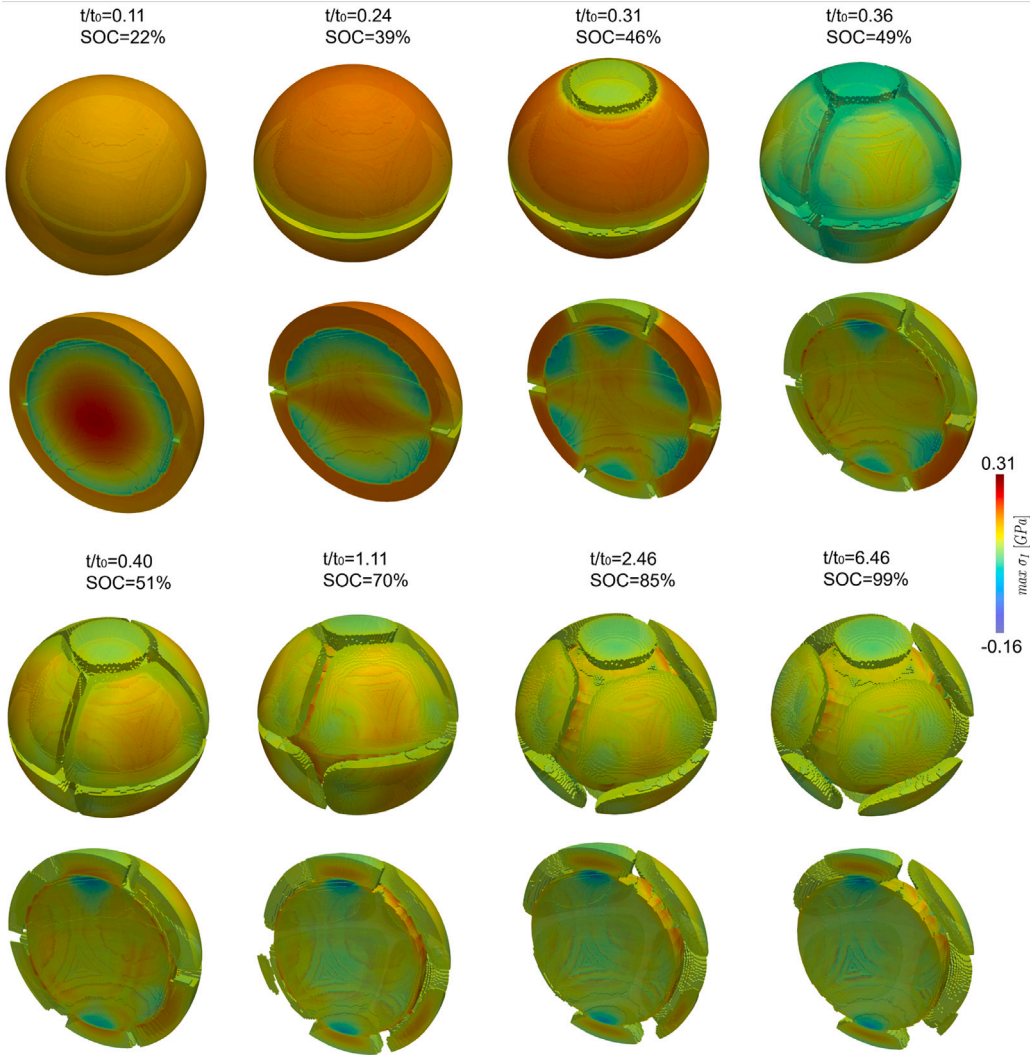

Fig. 10. The maximum principal stress σ_I during Li insertion in a 3D spherical storage particle embedded in the SE with $R_2 = 5$ µm, $a = 0.21$ µm and $i_p = 2$ A/m^2. For better visibility, only a half of the 3D spherical storage particle embedded in the SE is shown in the second and fourth rows. Regions with $d > 0.95$ are removed to show the location of the crack, and iso-surface visualization is used for better visibility.

on a time scale controlled by inertia effects, contributing to the dramatic drop in the maximum principal stress after the initiation of crack growth. Thereafter the remaining stress is due only to the inhomogeneous volume expansion of the AM constrained by the SE.

Due to the fast time scale of the unstable crack growth, the blocking effect of the crack on ionic conduction in the SE does not adjust simultaneously with the damage field. Only after crack propagation has ended does the above blocking effect of the crack become apparent. As a result, the maximum principal stress still exhibits a short, general trend of further decrease before there is another peak, see Fig. 13d.

Once the SOC reaches 46% ($t/t_0 = 0.31$), two additional cracks having cone shape are abruptly nucleated from the top and bottom part of the SE, which is associated with the second peak of the stress curve at B in Fig. 13d. Again, the highest value anywhere of the maximum principal stress immediately drops rapidly thereafter due to inertia driven crack propagation. However, when the SOC increases to 49% ($t/t_0 = 0.36$), the build-up of stress leads to crack branching perpendicular to the conical crack faces, which is associated with the third peak of the stress curve at C in Fig. 13d. Four new splitting cracks perpendicular to the top conical crack face propagate in an unstable way to the equator of the SE accompanied by the propagation of two new ones perpendicular to the bottom conical crack face. In contrast to the study on crack branching in storage particles during Li insertion (Klinsmann et al., 2016b), this branching in the SE is not caused by inertia effects but stems solely from the distribution of mechanical stress induced by the volume expansion of the storage particle constrained by the SE. The splitting cracks separate the top half of the SE into 5 segments. When the SOC approaches 51% ($t/t_0 = 0.40$), another two new splitting cracks perpendicular to the bottom conical crack

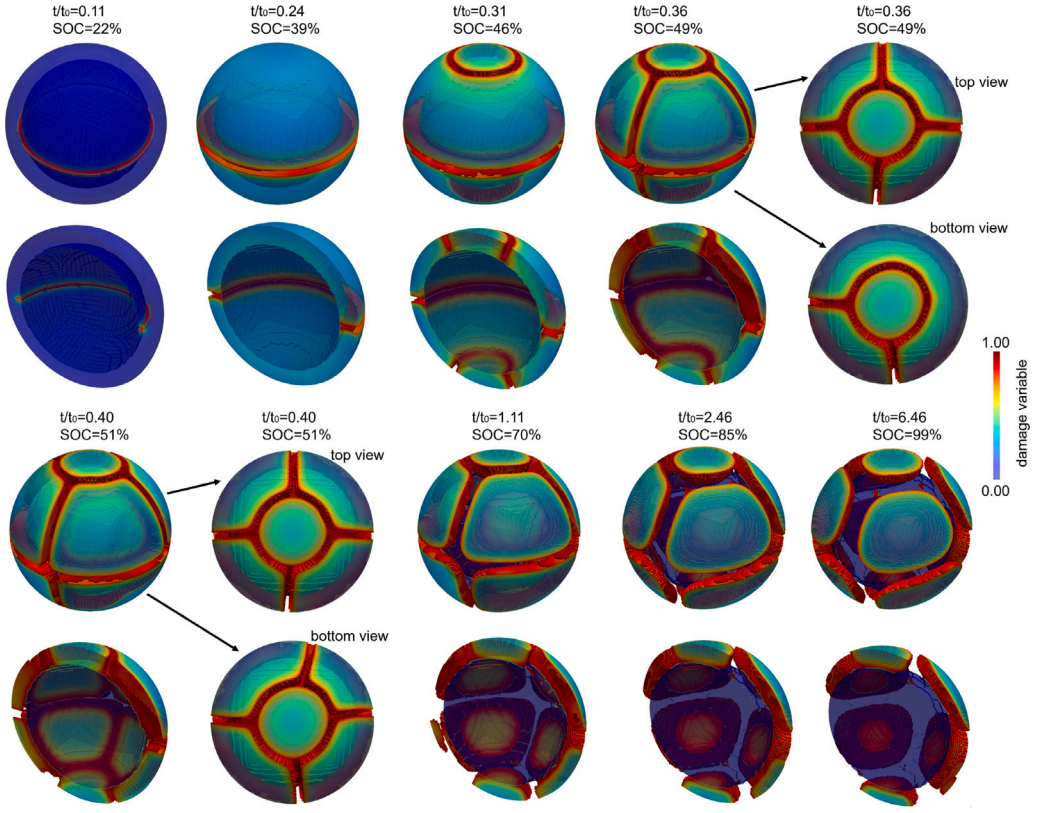

Fig. 11. Damage variable d during Li insertion in a 3D spherical storage particle embedded in the SE with $R_2 = 5$ μm, $a = 0.21$ μm and $i_p = 2$ A/m^2. For better visibility, only a half of the 3D spherical storage particle embedded in the SE is shown in the second and fourth rows. The top and bottom views for SOC = 49% and SOC = 51% are shown, see the arrow direction. Regions with $d > 0.95$ are removed to show the location of the crack, and iso-surface visualization is used for better visibility.

face propagate towards the equator of the SE, which is associated with the fourth peak of the stress curve at D in Fig. 13d. As a consequence, the bottom part of the SE is separated into 5 segments as well. Notice that the 8 splitting cracks described above do not entirely penetrate to the interface, such that the segments are still joined to each other by thin ligaments.

Considering the small width of the ligaments, what will happen as insertion goes on? As illustrated in Fig. 11, the crack deflects into the interface and interface delamination emerges in a stable way. This is marked by the noticeable decrease in the slope of SOC due to stable delamination, see Fig. 13a. The stable delamination destroys the ligaments between SE segments, and tears them apart. At full insertion ($t/t_0 = 6.46$), the SE finally breaks into 10 parts, while the storage particle does not completely detach from the SE since each part still is in contact with the storage particle via thin ligaments, see Fig. 11. We find that complex 3D crack patterns in the SE can be formed during insertion as a result of SE breakage, additional crack growth, crack branching and stable delamination, when growth of one or several cracks does not relieve enough tensile stress to keep further cracks from growing. Under these conditions the SE can break into several parts in just a half cycle.

According to the discussion above, SE cracking happens quite readily and takes place for all input parameters shown in Table 4. In order to explain this, we perform the following analytic assessments. The equations used hereby are based on very simplified assumptions and shall only serve for a qualitative understanding of SE cracking.

As before, the separation of the interface between the AM and the SE is assumed to be negligible. According to Deshpande and McMeeking (2023), the circumferential stress in the SE at the interface is given by

$$T_{se} = \frac{\frac{1}{3}\varepsilon^s(1+2f)E_{se}}{(1+\nu_{se})+2(1-2\nu_{se})f+2(1-2\nu_{am})(1-f)\frac{E_{se}}{E_{am}}}, \tag{51}$$

The tensile circumferential stress increases with distance from the interface, and is thus larger than the result in Eq. (51). Thus, the crack will grow into a rising stress field and its propagation will be unstable. This is consistent with our simulated unstable crack growth behavior.

In the absence of details of the crack shape, the stress intensity factor for the crack is approximated as Tada (2000)

$$K_I = T_{se}\sqrt{\pi a}. \tag{52}$$

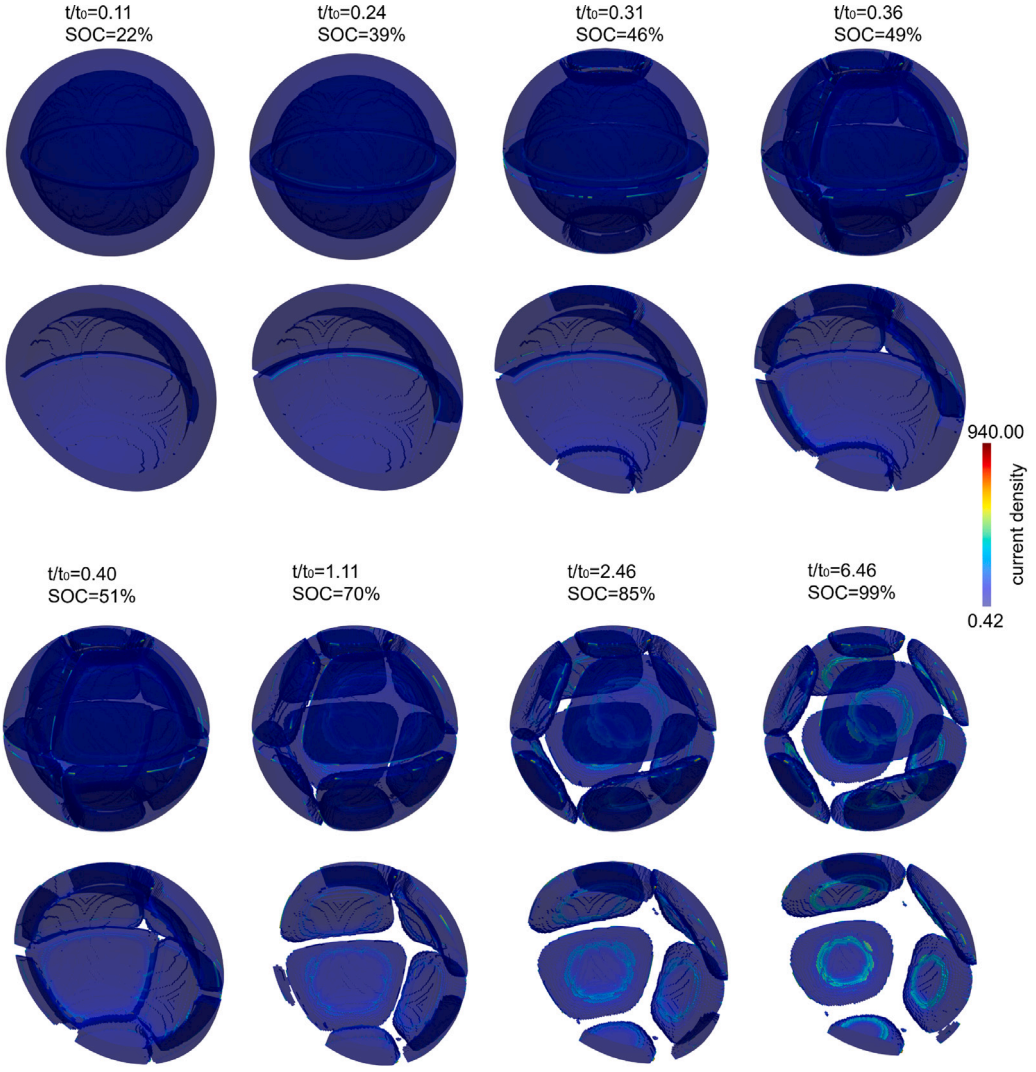

Fig. 12. Normalized current density during Li insertion in a 3D spherical storage particle embedded in the SE with $R_2 = 5$ μm, $a = 0.21$ μm and $i_p = 2$ A/m^2. For better visibility, only a half of the 3D spherical storage particle embedded in the SE is shown in the second and fourth rows. Regions with $d > 0.95$ are removed to show the location of the crack, and iso-surface visualization is used for better visibility.

The energy release rate related to the stress intensity factor is (Deshpande and McMeeking, 2023)

$$G = \frac{(1 - \nu_{se}^2)K_I^2}{E_{se}}. \tag{53}$$

To predict crack growth we set the energy release rate be equal to the critical energy release rate, G_c, and combine Eq. (51) with Eqs. (52) and (54) to predict the critical particle volume expansion given by

$$\varepsilon_T^s = \frac{3[(1+\nu_{se})E_{am} + 2(1-2\nu_{se})fE_{am} + 2(1-2\nu_{am})(1-f)E_{se}]}{(1+2f)E_{am}E_{se}} \cdot \sqrt{\frac{E_{se}G_c}{\pi d(1-\nu_{se}^2)}}. \tag{54}$$

If we apply the material parameters for $LiMn_2O_4$ and $75Li_2S{\cdot}25P_2S_5$ glass in Table 2 into Eq. (54) with $f = 0.5$, the critical particle volume expansion to propagate the crack will be approximately 1.1%. Therefore, the volume change of 7.3% (Hunter, 1981) for $LiMn_2O_4$ is higher than the critical particle volume expansion, such that it is quite likely for SE cracking to be associated with expansion of $LiMn_2O_4$. As a result, all input parameters in Table 4 lead to SE cracking, including SE breakage, crack branching and even additional crack growth.

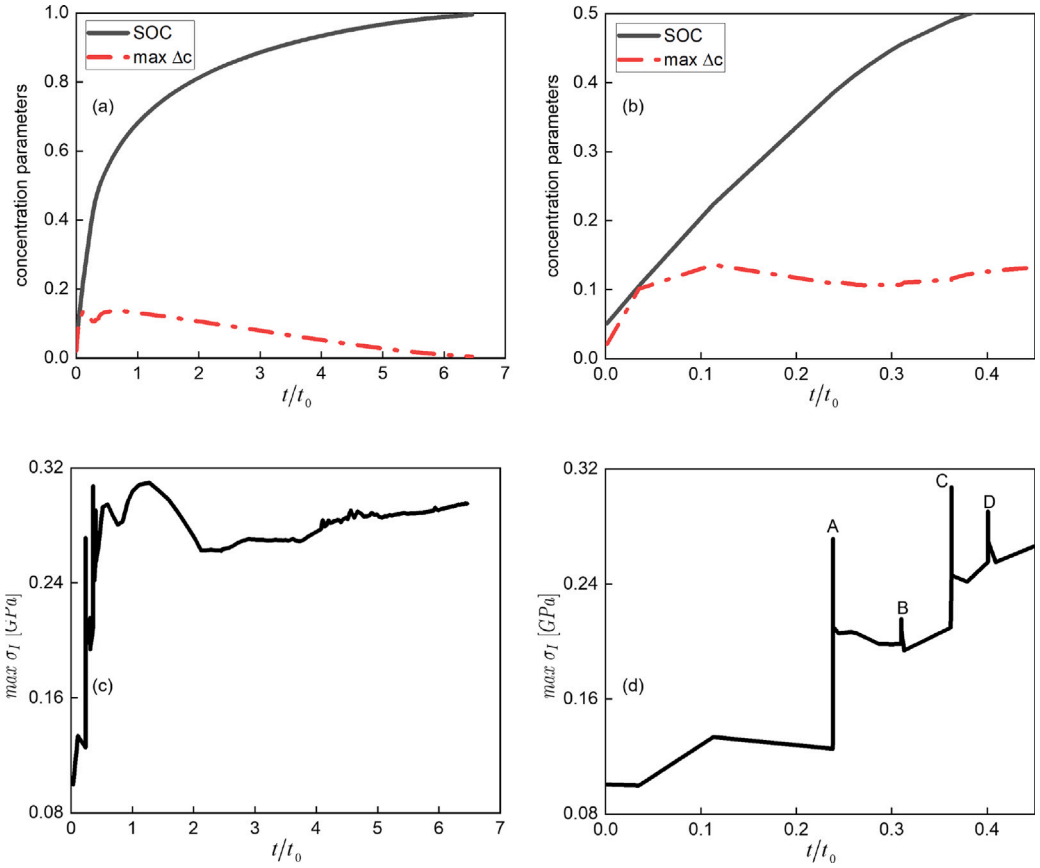

Fig. 13. Characteristic results for Li insertion with $R_2 = 5$ μm, $a = 0.21$ μm and $i_p = 2$ A/m^2 as a function of time. (a) SOC and maximum concentration difference $max\ \Delta c$ in units of maximum concentration c_{max}. (b) Magnified view of the SOC and maximum concentration difference $max\ \Delta c$. (c) The highest value of the maximum principal stress $max\ \sigma_I$. (d) Magnified view of the highest value of the maximum principal stress $max\ \sigma_I$ showing four distinct peaks of the stress curve labeled 'A', 'B', 'C', and 'D', respectively. These peaks are associated with unstable crack growth.

4.3.2. Electrolyte comminution

In order to examine whether or not comminution of the SE can take place during insertion, we investigate the parameter combination with larger SE sizes and higher applied current densities, as depicted in Fig. 14. Under these severe conditions, a larger maximum concentration difference arising in the storage particle leads to a higher stress level. As seen in Table 4, the SE can break into more parts for higher applied current densities i_p and larger SE sizes R_2. This is attributed to the fact that further branching in the SE occurs to separate the existing segments in the above severe conditions. For example, for the parameter combination with $R_2 = 5$ μm, $a = 0.21$ μm and $i_p = 20$ A/m^2 in Fig. 14a, further branching separates the existing segment into two smaller segments S1 and S2, leading to 12 segments of the SE. For the most severe condition of $R_2 = 20$ μm, $a = 0.21$ μm and $i_p = 20$ A/m^2, the SE finally breaks into 21 fragments, and the storage particle completely detaches from the SE, see Fig. 14d. Thus the SE with a larger size and a higher applied current density can break into many small parts in only one insertion half cycle and even make a complete comminution of the SE possible.

It should be noticed that, the model with a shell of SE around a particle is somewhat different from AM particles embedded in a continuous matrix. Therefore, the SE between neighboring particles is likely experience crack growth and fracture similar to the simulations and that extensive cracking and comminution of the SE is a likely outcome, but now with comminuted SE surrounding the AM particles in the composite cathode. Also, we judge the delamination simulations to be directly valid as the effect of the free surface around the model will not be a big influence on the results. Different from the cohesive zone models, we exploit the phase-field fracture approach to present interface delamination. The damage variable defined at the interface between the storage particle and the SE describes interface delamination. For Li extraction, the initial crack is introduced at the interface through the damage variable by defining an initially non-zero history field. As Li extraction goes on, the tensile stress at the crack tip becomes large enough to initiate delamination. Our simulations are consistent with analytic considerations based on the elastic fracture mechanics for interfacial cracks (Rice, 1988). The methodology used for the simulation requires the fracture to propagate along the interface between the storage particle and the SE. This behavior means that the interface effectively has a lower fracture toughness than the SE further away from the interface. The fact that the delamination is technically in the SE, albeit very close to the interface, does not mean that the fracture toughness of the interface is identical to that of the SE.

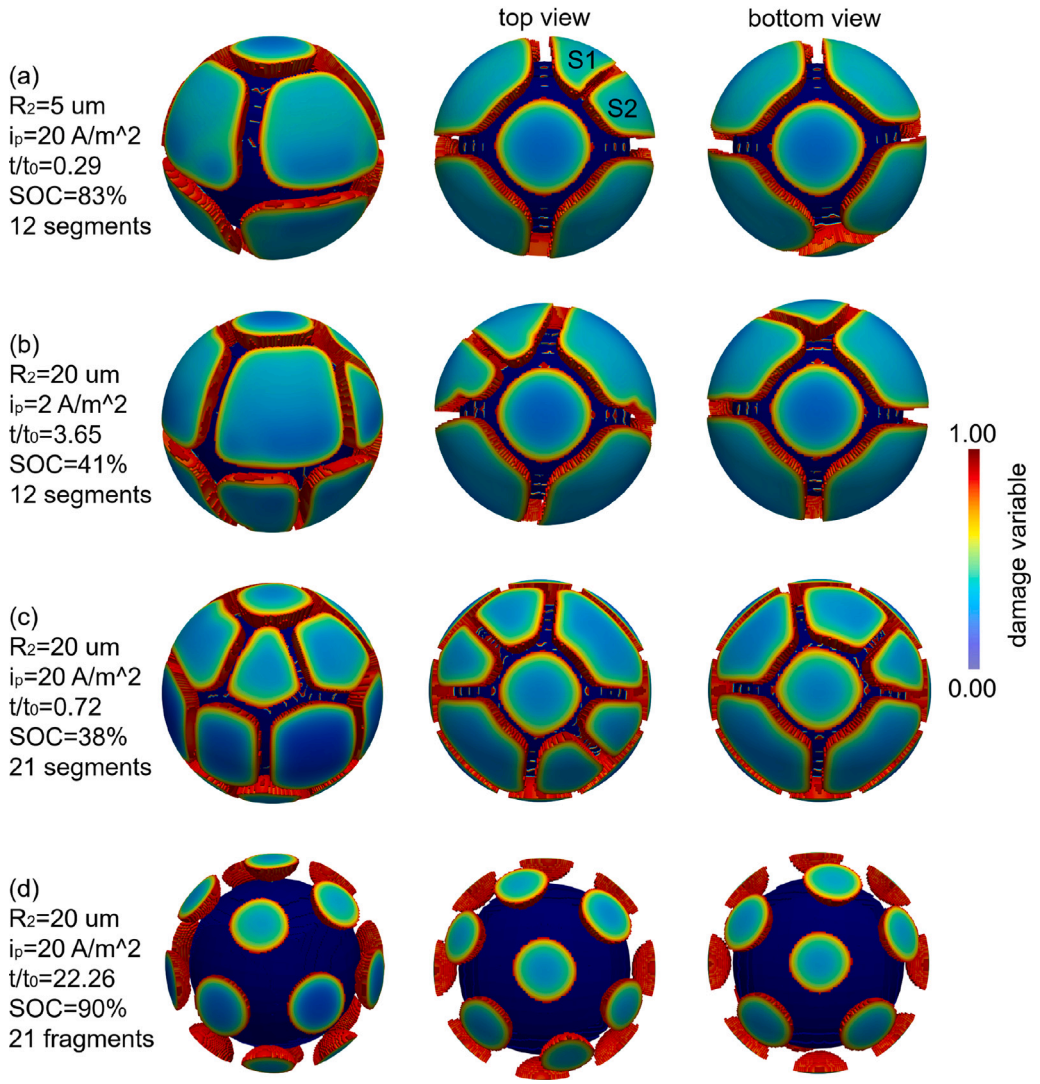

Fig. 14. Crack patterns in 3D spherical storage particles embedded in the SE after crack branching during Li insertion. (a) $R_2 = 5$ μm, $a = 0.21$ μm and $i_p = 20$ A/m^2. (b) $R_2 = 20$ μm, $a = 0.21$ μm and $i_p = 2$ A/m^2. (c–d) $R_2 = 20$ μm, $a = 0.21$ μm and $i_p = 20$ A/m^2. For better visibility, the top and bottom views for the first column are shown in the second and third columns, respectively. S1 and S2 represent two smaller segments. Regions with $d > 0.95$ are removed to show the location of the crack.

To capture different crack phenomena, we investigate exhaustive series of studies of full 3D spherical particles embedded in SE. As the current flows into/out of the SE at its perimeter, Li will be inserted/extracted from the storage particle via interfacial reaction. The flux of Li into/out of storage particles at the AM/SE interface not only depends on the applied current density at the outer surface of SE, but also on the SE size and the interfacial defect size due to damage dependent interfacial reaction. Since complete delamination happens at different SOC_{ck} prior to the fully delithiated state, it is difficult to calculate the average extraction rate for different extraction cases. In order to better understand how fast Li will be extracted, we calculate the real time t_{ck} when crack growth is initiated, see Table 3. t_{ck} also represents the required time for complete delamination due to the unstable crack growth. We can find that t_{ck} falls into the range between 0.038 h and 55.94 h for the extraction cases. For example, for Li extraction with $R_2 = 5$ μm and $a = 1.25$ μm, it takes 2.10 h for $i_p = 2$ A/m^2 to reach complete delamination but 0.13 h for $i_p = 20$ A/m^2. Most of the extraction cases need more than 0.25 h for complete delamination. On the other hand, for the insertion cases with $R_2 = 5$ μm, the SE breaks into several parts when the time reaches 6.34 h, 1.33 h and 0.28 h, respectively, for $i_p = 2$ A/m^2, $i_p = 10$ A/m^2 and $i_p = 20$ A/m^2. While for the insertion cases with $R_2 = 20$ μm, it takes 140.46 h, 64.03 h, and 21.97 h, respectively, to make SE comminution for $i_p = 2$ A/m^2, $i_p = 10$ A/m^2 and $i_p = 20$ A/m^2. Furthermore, we also calculate the initial C-rate C based on the initial applied current, see Tables 3 and 4, respectively, for extraction and insertion. We can see that C falls into the range between 0.17 and 26.79 for the extraction cases, and the range between 0.98 and 39.10 for the insertion cases. Therefore, all the insertion and extraction cases in our work are not beyond reasonable situations.

We here assume the storage particle is completely surrounded by the SE. This may not describe the actual situation perfectly, but nevertheless provides a good first approximation in absence of physically sound information on that which part of the storage particle is surrounded by the SE. Indeed, this assumption has been widely made on the modeling of the interaction between the storage particle and the SE. For example, in 1D analytical models (Bucci et al., 2018, 2017a), even in the 2D simulation of the composite electrode (Bistri and Di Leo, 2021). On the other hand, we focus on a full 3D spherical particle embedded in the SE rather than the electrode level. For the purpose of achieving representative statements, the geometry of concentric spheres of the AM and the SE is employed. In our particle level, we mainly investigate the shrinkage and swelling of a single storage particle confined by the surrounding SE when lithium is extracted or inserted, ignoring interactions with surrounding storage particles and the SE in the rest of the electrode. The above interactions can have a significant effect on the cracking behavior at the electrode level. The composite electrode modeling is beyond the scope of the current work, please refer to Bucci et al. (2017b), Bistri and Di Leo (2021) for details regarding the modeling of this aspect. Despite the above assumption, our modeling predictions on the storage particle delamination and SE cracking exhibit a favorable comparison with analytic considerations (Deshpande and McMeeking, 2023). In our future work, we will extend the current particle model into an electrode model accounting for the interactions with surrounding storage particles and the SE in the rest of the electrode. It should be mentioned that initial studies on single particles are helpful before building on them for more intricate models in terms of geometry. On the other hand, studying the difference in fracture between particles that are partially covered by SE with different contact areas would allow for a more realistic scenario. Accordingly, this will be our future work direction.

5. Conclusions

An electro-chemo-mechanical fracture model of Li diffusion, ionic conduction, interfacial reaction, mechanical stress and crack growth is presented using a phase field fracture approach for the storage particle embedded in the SE in cathodes of SSBs. The approach allows the study of the behavior of Li diffusion in the AM, ionic conduction in the SE, electrochemical reaction at the interface, and crack growth, as well as their mutual interaction, in a simultaneous fashion. This is the first time a full 3D dynamical description of interface delamination and SE cracking for storage particles embedded in solid electrolytes is presented.

Interface delamination is strongly affected by interfacial defect sizes due to damage dependent interfacial reaction. Although material properties are assumed to provide a setting that is as simple as possible, i.e., isotropic diffusion, the absence of phase changes, and much more, the interplay of Li diffusion, ionic conduction, interfacial reaction and fracture, as well as the resulting crack topologies, become rather complex.

We find that interface delamination is a very likely event during extraction, which happens in an unstable way until complete debonding. Damage dependent interfacial reaction leads to greater Li concentration and higher current density at the cracked interface region. Homogeneous delamination can emerge for small interfacial defects with larger particle sizes and higher applied current densities. A smaller interfacial defect leads to the striking behavior that less time is required to initiate delamination due to a higher total rate of Li extraction. More particle storage capacity can be utilized for smaller particle sizes and smaller interfacial defects prior to delamination.

It is further demonstrated that SE cracking can happen quite readily during insertion. Complex fracture phenomena, such as, crack branching and SE breakage, can break the SE into several parts in only one insertion half cycle. Higher applied current densities and larger particle sizes even make complete delamination a possible event during insertion, leading to a complete comminution of the SE.

CRediT authorship contribution statement

Tao Zhang: Writing – review & editing, Writing – original draft, Software, Methodology, Investigation, Formal analysis, Data curation, Conceptualization. **Marc Kamlah:** Writing – review & editing, Supervision, Project administration, Funding acquisition, Conceptualization. **Robert M. McMeeking:** Writing – review & editing, Supervision, Project administration, Conceptualization.

Declaration of competing interest

The authors declare that they have no known competing financial interests or personal relationships that could have appeared to influence the work reported in this paper.

Data availability

Data will be made available on request.

Acknowledgments

Support by the state of Baden-Württemberg, Germany through bwHPC is gratefully acknowledged. This work contributes to the research performed at CELEST (Center for Electrochemical Energy Storage Ulm-Karlsruhe) and was cofunded by the German Research Foundation (DFG), Germany under Project ID 390874152 (POLiS Cluster of Excellence, EXC 2154).

Appendix A. Weak form of the boundary-value problem

For the SE, we multiply the field Eqs. (6), (16) and (19) with variational test functions $\delta\phi$, δd and $\delta\vec{u}$ as used in Galerkin's method, and integrate over the full body B_{se}. With the help of Eq. (21), the field Eq. (6) yields

$$\begin{aligned} G^{se}_{\phi}(\phi,d) \;=\; & -\int_{B_{se}} \operatorname{div}\big(((1-d)^{\alpha}\kappa_0 + d^{\alpha}(\beta_1 \boldsymbol{D} \\ & +\beta_2(\boldsymbol{I}-\boldsymbol{D})\kappa_0))\nabla\phi\big)\delta\phi \; dV = 0, \end{aligned} \tag{A.1}$$

which depends on the damage field through the crack dependent ionic conduction. Applying the divergence theorem and integration by parts, we rearrange the above weak form to

$$\begin{aligned} G^{se}_{\phi}(\phi,d) \;=\; & \int_{B_{se}} ((1-d)^{\alpha}\kappa_0 + d^{\alpha}(\beta_1 \boldsymbol{D} + \beta_2(\boldsymbol{I}-\boldsymbol{D})\kappa_0))\nabla\phi\cdot\nabla(\delta\phi)\; dV \\ & -\int_{\partial B_{se}} ((1-d)^{\alpha}\kappa_0 + d^{\alpha}(\beta_1 \boldsymbol{D} + \beta_2(\boldsymbol{I}-\boldsymbol{D})\kappa_0))\nabla\phi\cdot\vec{n}\delta\phi \; dA \\ & = 0. \end{aligned} \tag{A.2}$$

Following the same procedure for Eq. (6), the weak form of the evolution equation for the damage field reads

$$\begin{aligned} G^{se}_{d}(d,\vec{u}) \;=\; & \int_{B_{se}} (\eta\frac{\partial d}{\partial t} - 2(1-d)H_{se} + \frac{G_c}{l}d)\delta d + G^{se}_{c}\; l\; \nabla d\cdot\nabla(\delta d)\; dV \\ & -\int_{\partial B_{se}} G^{se}_{c}\; l\; \nabla d\cdot\vec{n}\delta d\; dA = 0, \end{aligned} \tag{A.3}$$

which depends on the displacement field through the history field H_{se}. The weak form of Eq. (19) describing the balance of linear momentum reads

$$\begin{aligned} G^{se}_{\vec{u}}(\vec{u},d) \;=\; & \int_{B_{se}} \mathbf{T}_{se} : \nabla(\delta\vec{u})\; dV - \int_{\partial B_{se}} \mathbf{T}\cdot\vec{n}\cdot\delta\vec{u}\; dA \\ & +\int_{B_{se}} \rho_{se}\frac{\partial^2\vec{u}}{\partial t^2}\delta\vec{u}\; dV = 0. \end{aligned} \tag{A.4}$$

The dependence of $G^{se}_{\vec{u}}(\vec{u},d)$ on the damage field results from the definition of the stress tensor $\mathbf{T}_{se}$.

As for the AM, we multiply the field Eqs. (27), (32) and (33) with variational test functions δc, $\delta\mu$ and $\delta\vec{u}$, and integrate over the full body B_{am}. For the field Eq. (27) resulting from the mixed formulation, we obtain

$$\begin{aligned} G^{am}_{c}(c,\mu,\vec{u}) \;=\; & \int_{B_{am}} (\mu_0 + RT\left(\ln(c/c_{max}) - \ln\left(1-c/c_{max}\right)\right) \\ & -\Omega T^{am}_{H})\; \delta c\; dV - \int_{B_{am}} \mu\delta c\; dV = 0, \end{aligned} \tag{A.5}$$

which depends on the displacement through the elastic strain energy density. Applying the divergence theorem and by integration by parts, the balance of mass (32) yields

$$\begin{aligned} G^{am}_{\mu}(\mu,c) \;=\; & \int_{B_{am}} \frac{\partial c}{\partial t}\delta\mu\; dV + \int_{B_{am}} c\mathbf{M}(c)\,\nabla\mu\cdot\nabla(\delta\mu)\; dV \\ & -\int_{\partial B_{am}} c\mathbf{M}(c)\,\nabla\mu\cdot\vec{n}\delta\mu\; dA = 0. \end{aligned} \tag{A.6}$$

The weak form of Eq. (33) describing the balance of linear momentum reads

$$\begin{aligned} G^{am}_{\vec{u}}(\vec{u},c) \;=\; & \int_{B_{am}} \mathbf{T}_{am} : \nabla(\delta\vec{u})\; dV - \int_{\partial B_{am}} \mathbf{T}\cdot\vec{n}\cdot\delta\vec{u}\; dA \\ & +\int_{B_{am}} \rho_{am}\frac{\partial^2\vec{u}}{\partial t^2}\delta\vec{u}\; dV = 0. \end{aligned} \tag{A.7}$$

The dependence of $G^{am}_{\vec{u}}(\vec{u},c)$ on the concentration results from the definition of the stress tensor $\mathbf{T}_{am}$.

Appendix B. Validation of linearized Butler–Volmer interfacial reaction

The assumption of linearized Butler–Volmer interfacial reaction is directly dependent on the exchange current density. To verify that the applied current densities are always lower than the exchange current densities at the interface for all the simulation cases, we calculate the minimum value of the exchange current density at the intact part of the interface using

$$i_{0min} = i_{00}exp\left(\frac{(1-\beta)\mu_{se}}{RT}\right)exp\left(\frac{\beta\mu_{min}}{RT}\right). \tag{B.1}$$

with $i_{00} = 30\ \mathrm{A/m^2}$, $\beta = 0.5$, and $\mu_{se} = 0$. Here, μ_{min} is the minimum value of the chemical potential at the interface.

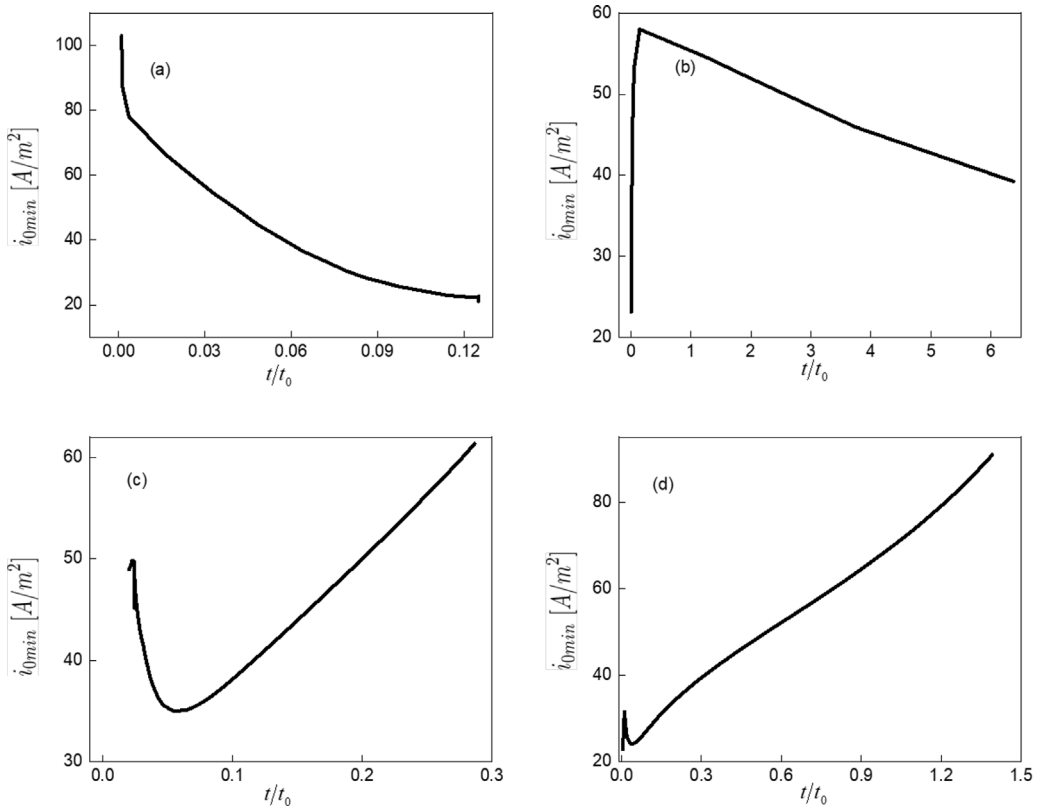

Fig. B.15. The minimum value of the exchange current density for the extraction and insertion cases with $i_p = 20$ A/m^2 as a function of time. (a) Li extraction with $R_2 = 5$ μm and $a = 1.25$ μm. (b) Li extraction with $R_2 = 20$ μm and $a = 1.25$ μm. (c) Li insertion with $R_2 = 5$ μm and $a = 0.21$ μm. (d) Li insertion with $R_2 = 20$ μm and $a = 0.21$ μm.

As shown in Fig. B.15, the highest applied current density ($i_p = 20$ A/m^2) are always lower than the minimum value of the exchange current density for both extraction and insertion cases. We also calculate the cases with lower applied current density ($i_p = 2$ A/m^2 and $i_p = 10$ A/m^2). They also definitely obey the linearized regime of the Butler–Volmer equation (we do not show the results here). Thus, the exchange current density constant $i_{00} = 30$ A/m^2 is large enough to ensure that the linearized solution is valid for all the simulation cases.

References

Amanieu, H.Y., Rosato, D., Sebastiani, M., Massimi, F., Lupascu, D.C., 2014. Mechanical property measurements of heterogeneous materials by selective nanoindentation: Application to $LiMn_2O_4$ cathode. Mater. Sci. Eng. A 593, 92–102.

Bhandakkar, T.K., Gao, H., 2010. Cohesive modeling of crack nucleation under diffusion induced stresses in a thin strip: Implications on the critical size for flaw tolerant battery electrodes. Int. J. Solids Struct. 47 (10), 1424–1434.

Bistri, D., Afshar, A., Di Leo, C.V., 2021. Modeling the chemo-mechanical behavior of all-solid-state batteries: A review. Meccanica 56, 1523–1554.

Bistri, D., Di Leo, C.V., 2021. Modeling of chemo-mechanical multi-particle interactions in composite electrodes for liquid and solid-state Li-ion batteries. J. Electrochem. Soc. 168 (3), 030515.

Bistri, D., Di Leo, C.V., 2023. A continuum electro-chemo-mechanical gradient theory coupled with damage: Application to Li-metal filament growth in all-solid-state batteries. J. Mech. Phys. Solids 174, 105252.

Borden, M.J., Hughes, T.J., Landis, C.M., Verhoosel, C.V., 2014. A higher-order phase-field model for brittle fracture: Formulation and analysis within the isogeometric analysis framework. Comput. Methods Appl. Mech. Engrg. 273, 100–118.

Borden, M.J., Verhoosel, C.V., Scott, M.A., Hughes, T.J., Landis, C.M., 2012. A phase-field description of dynamic brittle fracture. Comput. Methods Appl. Mech. Engrg. 217, 77–95.

Bucci, G., Swamy, T., Bishop, S., Sheldon, B.W., Chiang, Y.M., Carter, W.C., 2017a. The effect of stress on battery-electrode capacity. J. Electrochem. Soc. 164 (4), A645.

Bucci, G., Swamy, T., Chiang, Y.M., Carter, W.C., 2017b. Modeling of internal mechanical failure of all-solid-state batteries during electrochemical cycling, and implications for battery design. J. Mater. Chem. A 5 (36), 19422–19430.

Bucci, G., Talamini, B., Balakrishna, A.R., Chiang, Y.M., Carter, W.C., 2018. Mechanical instability of electrode-electrolyte interfaces in solid-state batteries. Phys. Rev. Mater. 2 (10), 105407.

Cheng, E.J., Sharafi, A., Sakamoto, J., 2017. Intergranular Li metal propagation through polycrystalline $Li_{6.25}Al_{0.25}La_3Zr_2O_{12}$ ceramic electrolyte. Electrochim. Acta 223, 85–91.

Christensen, J., Newman, J., 2006. A mathematical model of stress generation and fracture in lithium manganese oxide. J. Electrochem. Soc. 153 (6), A1019.

Crank, J., 1979. The Mathematics of Diffusion. Oxford University Press.

Deshpande, V.S., McMeeking, R.M., 2023. Models for the Interplay of Mechanics, Electrochemistry, Thermodynamics, and Kinetics in Lithium-Ion Batteries. Appl. Mech. Rev. 75 (1), 010801.

Ganser, M., Hildebrand, F.E., Kamlah, M., McMeeking, R.M., 2019a. A finite strain electro-chemo-mechanical theory for ion transport with application to binary solid electrolytes. J. Mech. Phys. Solids 125, 681–713.

Ganser, M., Hildebrand, F.E., Klinsmann, M., Hanauer, M., Kamlah, M., McMeeking, R.M., 2019b. An extended formulation of butler-volmer electrochemical reaction kinetics including the influence of mechanics. J. Electrochem. Soc. 166 (4), H167.

Garcıa, R.E., Chiang, Y.M., Carter, W.C., Limthongkul, P., Bishop, C.M., 2004. Microstructural modeling and design of rechargeable lithium-ion batteries. J. Electrochem. Soc. 152 (1), A255.

Gaston, D., Newman, C., Hansen, G., Lebrun-Grandie, D., 2009. MOOSE: A parallel computational framework for coupled systems of nonlinear equations. Nucl. Eng. Des. 239 (10), 1768–1778.

Huggins, R., Nix, W., 2000. Decrepitation model for capacity loss during cycling of alloys in rechargeable electrochemical systems. Ionics 6, 57–63.

Hunter, J.C., 1981. Preparation of a new crystal form of manganese dioxide: λ-MnO_2. J. Solid State Chem. 39 (2), 142–147.

Janek, J., Zeier, W.G., 2016. A solid future for battery development. Nat. Energy 1 (9), 1–4.

Klinsmann, M., 2016. The Effects of Internal Stress and Lithium Transport on Fracture in Storage Materials in Lithium-Ion Batteries, Vol. 54. KIT Scientific Publishing.

Klinsmann, M., Hildebrand, F.E., Ganser, M., McMeeking, R.M., 2019. Dendritic cracking in solid electrolytes driven by lithium insertion. J. Power Sources 442, 227226.

Klinsmann, M., Rosato, D., Kamlah, M., McMeeking, R.M., 2015a. An assessment of the phase field formulation for crack growth. Comput. Methods Appl. Mech. Engrg. 294, 313–330.

Klinsmann, M., Rosato, D., Kamlah, M., McMeeking, R.M., 2015b. Modeling crack growth during Li extraction in storage particles using a fracture phase field approach. J. Electrochem. Soc. 163 (2), A102.

Klinsmann, M., Rosato, D., Kamlah, M., McMeeking, R.M., 2016a. Modeling crack growth during Li extraction and insertion within the second half cycle. J. Power Sources 331, 32–42.

Klinsmann, M., Rosato, D., Kamlah, M., McMeeking, R.M., 2016b. Modeling crack growth during Li insertion in storage particles using a fracture phase field approach. J. Mech. Phys. Solids 92, 313–344.

Koerver, R., Aygun, I., Leichtweiß, T., Dietrich, C., Zhang, W., Binder, J.O., Hartmann, P., Zeier, W.G., Janek, J., 2017. Capacity fade in solid-state batteries: interphase formation and chemomechanical processes in nickel-rich layered oxide cathodes and lithium thiophosphate solid electrolytes. Chem. Mater. 29 (13), 5574–5582.

Lin, D., Liu, Y., Cui, Y., 2017. Reviving the lithium metal anode for high-energy batteries. Nature Nanotechnol. 12 (3), 194–206.

McGrogan, F.P., Swamy, T., Bishop, S.R., Eggleton, E., Porz, L., Chen, X., Chiang, Y.M., Van Vliet, K.J., 2017. Compliant yet brittle mechanical behavior of $Li_2S--P_2S_5$ lithium-ion-conducting solid electrolyte. Adv. Energy Mater. 7 (12), 1602011.

Mesgarnejad, A., Karma, A., 2019. Phase field modeling of chemomechanical fracture of intercalation electrodes: Role of charging rate and dimensionality. J. Mech. Phys. Solids 132, 103696.

Miehe, C., Dal, H., Schänzel, L.M., Raina, A., 2016. A phase-field model for chemo-mechanical induced fracture in lithium-ion battery electrode particles. Internat. J. Numer. Methods Engrg. 106 (9), 683–711.

Miehe, C., Welschinger, F., Hofacker, M., 2010. Thermodynamically consistent phase-field models of fracture: Variational principles and multi-field FE implementations. Internat. J. Numer. Methods Engrg. 83 (10), 1273–1311.

Mukherjee, D., Hao, S., Shearing, P.R., McMeeking, R.M., Fleck, N.A., Deshpande, V.S., 2023. Ingress of Li into solid electrolytes: Cracking and sparsely filled cracks. Small Struct. 2300022.

Mykhaylov, M., Ganser, M., Klinsmann, M., Hildebrand, F., Guz, I., McMeeking, R., 2019. An elementary 1-dimensional model for a solid state lithium-ion battery with a single ion conductor electrolyte and a lithium metal negative electrode. J. Mech. Phys. Solids 123, 207–221.

Newmark, N.M., 1959. A method of computation for structural dynamics. J. Eng. Mech. Div. 85 (3), 67–94.

O'Connor, D., Welland, M.J., Liu, W.K., Voorhees, P.W., 2016. Phase transformation and fracture in single Li_xFePO_4 cathode particles: A phase-field approach to Li–ion intercalation and fracture. Modelling Simul. Mater. Sci. Eng. 24 (3), 035020.

Ortiz, M., Pandolfi, A., 1999. Finite-deformation irreversible cohesive elements for three-dimensional crack-propagation analysis. Internat. J. Numer. Methods Engrg. 44 (9), 1267–1282.

Pasta, M., Armstrong, D., Brown, Z.L., Bu, J., Castell, M.R., Chen, P., Cocks, A., Corr, S.A., Cussen, E.J., Darnbrough, E., et al., 2020. 2020 Roadmap on solid-state batteries. J. Phys.: Energy 2 (3), 032008.

Porz, L., Swamy, T., Sheldon, B.W., Rettenwander, D., Frömling, T., Thaman, H.L., Berendts, S., Uecker, R., Carter, W.C., Chiang, Y.M., 2017. Mechanism of lithium metal penetration through inorganic solid electrolytes. Adv. Energy Mater. 7 (20), 1701003.

Rice, J., 1988. Elastic fracture mechanics concepts for interfacial cracks. J. Appl. Mech. 55 (1), 98–103.

Sakuda, A., Hayashi, A., Takigawa, Y., Higashi, K., Tatsumisago, M., 2013a. Evaluation of elastic modulus of $Li_2S--P_2S_5$ glassy solid electrolyte by ultrasonic sound velocity measurement and compression test. J. Ceram. Soc. Japan 121 (1419), 946–949.

Sakuda, A., Hayashi, A., Tatsumisago, M., 2013b. Sulfide solid electrolyte with favorable mechanical property for all-solid-state lithium battery. Sci. Rep. 3 (1), 2261.

Shishvan, S., Fleck, N., McMeeking, R., Deshpande, V., 2020a. Dendrites as climbing dislocations in ceramic electrolytes: Initiation of growth. J. Power Sources 456, 227989.

Shishvan, S., Fleck, N., McMeeking, R., Deshpande, V., 2020b. Growth rate of lithium filaments in ceramic electrolytes. Acta Mater. 196, 444–455.

Tada, H., 2000. Stress analysis results for common test specimen configurations. In: The Stress Analysis of Cracks Handbook. ASME Press.

Xu, X.-P., Needleman, A., 1994. Numerical simulations of fast crack growth in brittle solids. J. Mech. Phys. Solids 42 (9), 1397–1434.

Xu, R., Zhao, K., 2018. Corrosive fracture of electrodes in Li-ion batteries. J. Mech. Phys. Solids 121, 258–280.

Xu, B.X., Zhao, Y., Stein, P., 2016. Phase field modeling of electrochemically induced fracture in Li-ion battery with large deformation and phase segregation. GAMM-Mitt. 39 (1), 92–109.

Yang, C., Fu, K., Zhang, Y., Hitz, E., Hu, L., 2017. Protected lithium-metal anodes in batteries: From liquid to solid. Adv. Mater. 29 (36), 1701169.

Zhang, W., Richter, F.H., Culver, S.P., Leichtweiss, T., Lozano, J.G., Dietrich, C., Bruce, P.G., Zeier, W.G., Janek, J., 2018. Degradation mechanisms at the $Li_{10}GeP_2S_{12}/LiCoO_2$ cathode interface in an all-solid-state lithium-ion battery. ACS Appl. Mater. Interfaces 10 (26), 22226–22236.

Zhang, X., Shyy, W., Sastry, A.M., 2007. Numerical simulation of intercalation-induced stress in Li-ion battery electrode particles. J. Electrochem. Soc. 154 (10), A910.

Zhang, T., Sotoudeh, M., Groß, A., McMeeking, R.M., Kamlah, M., 2023. 3D microstructure evolution in $NaxFePO_4$ storage particles for sodium-ion batteries. J. Power Sources 565, 232902.

Zuo, P., Zhao, Y.P., 2015. A phase field model coupling lithium diffusion and stress evolution with crack propagation and application in lithium ion batteries. Phys. Chem. Chem. Phys. 17 (1), 287–297.